

The XXL survey: XL. Obscuration properties of red AGN in XXL – N

V. A. Masoura^{1,2}, I. Georgantopoulos¹, G. Mountrichas^{3,1}, C. Vignali^{4,5}, E. Koulouridis^{1,6}, L. Chiappetti⁷, S. Fotopoulou⁸, S. Paltani⁹, M. Pierre⁶

¹ National Observatory of Athens, V. Paulou & I. Metaxa, 15 236 Penteli, Greece e-mail: vmasoura@noa.gr

² Section of Astrophysics, Astronomy and Mechanics, Department of Physics, Aristotle University of Thessaloniki, 54 124, Thessaloniki, Greece

³ Instituto de Fisica de Cantabria (CSIC-Universidad de Cantabria), Avenida de los Castros, 39005 Santander, Spain

⁴ Dipartimento di Fisica e Astronomia, Alma Mater Studiorum, Università degli Studi di Bologna, Via Gobetti 93/2, I-40129 Bologna, Italy

⁵ INAF - Osservatorio di Astrofisica e Scienza dello Spazio di Bologna, Via Gobetti 93/3, I-40129 Bologna, Italy

⁶ AIM, CEA, CNRS, Université Paris-Saclay, Université Paris Diderot, Sorbonne Paris Cité, F-91191 Gif-sur-Yvette, France

⁷ INAF, IASF Milano, via Corti 12, 20133 Milano, Italy

⁸ Centre for Extragalactic Astronomy, Department of Physics, Durham University, Durham DH1 3LE, UK

⁹ Department of Astronomy, University of Geneva, ch. d' Écogia 16, CH-1290 Versoix, Switzerland

May 8, 2022

ABSTRACT

The combination of optical and mid-infrared (mid-IR) photometry has been extensively used to select red Active Galactic Nuclei (AGN). Our aim is to explore the obscuration properties of these red AGN with both X-ray spectroscopy as well as Spectral Energy Distributions (SEDs). In this study, we re-visit the relation between optical/mid-IR extinction and X-ray absorption. We use IR selection criteria, specifically the $W1$ and $W2$ WISE bands (Assef et al.), to identify 4798 AGN in the XMM – XXL area ($\sim 25 \text{ deg}^2$). Application of optical/mid-IR colours ($r - W2 > 6$) reveals 561 red AGN (14%). 47/561 have available X-ray spectra with at least 50 net (background-subtracted) counts per detector. For these sources, we construct SEDs from the optical to the mid-IR using the CIGALE code. The SED fitting shows that 44/47 sources present clear signs of obscuration, based on the AGN emission and the estimated inclination angle. SED fitting also reveals ten systems ($\sim 20\%$) which are dominated by the galaxy. In these cases, the red colours are attributed to the host galaxy rather than AGN absorption. Excluding these ten systems from our sample and applying X-ray spectral fitting analysis, shows that up to 76% (28/37) of the IR red AGN present signs of X-ray absorption. Thus, there are nine sources ($\sim 20\%$ of the sample) that although optically red, are not substantially X-ray absorbed. $\sim 50\%$ of these sources present broad emission lines in their optical spectra. We suggest that the reason for this apparent discrepancy is that the r - $W2$ criterion is sensitive to smaller amounts of obscuration relative to the X-ray spectroscopy. In conclusion, it appears that the majority of red AGN present considerable obscuration levels as shown by their SEDs. Their X-ray absorption is moderate with a mean of $N_H \sim 10^{22} \text{ cm}^{-2}$.

Key words. Extragalactic Astrophysics, IR AGN, Obscured AGN

1. Introduction

The vast majority of galaxies host a supermassive black hole (SMBH) in their centre (e.g. Kormendy et al. 1996a,b), with mass range from hundreds of thousands to billions solar masses ($\approx 10^5 - 10^{10} M_\odot$). When this SMBH grows releases huge amounts of energy across the electromagnetic spectrum and becomes visible as AGN. AGN have characteristic properties such as high luminosities (up to $L_{\text{bol}} \simeq 10^{48} \text{ ergs}^{-1}$) and rapid variability (e.g. Ulrich et al. 1997).

According to the unification scheme (Antonucci 1993) the central source of the AGN structure consists of the SMBH, the corona and the accretion disk. These regions are surrounded by an axisymmetric dusty structure in a toroidal shape (e.g. Netzer 2015). Starting from the inner part of the source, the X-ray and the optical/ultraviolet (UV) wavelengths are related to the corona and the accretion disk respectively (e.g. Wilkins & Gallo 2015; Haardt & Maraschi 1991). The torus is responsible for the infrared (IR) emission (e.g. Edelson & Malkan 1986), since the hot dust is related to the radiation in these wavelengths. There are

different torus models based on the distribution of dust, such as smooth (e.g. Fritz et al. 2006), clumpy (Nenkova et al. 2008a,b; Hönig & Kishimoto 2010; Hönig et al. 2010; Hönig & Kishimoto 2017) and a combination of these two (Siebenmorgen et al. 2015; Stalevski et al. 2016). Unified models propose that different observational classes of AGN are a single type of a physical object, observed at different viewing angles (e.g. different orientations of the observer with respect to the torus). Thus, Type 1 and Type 2 AGN refer to the face-on (unobscured) and edge-on (obscured) AGN, respectively. However, in the case of a clumpy torus the classification of the AGN type is not, necessarily, a consequence of the different viewing angles since the dust is not contributed homogeneously. Based on their optical/UV spectrum, Type 1 AGN present basically broad permitted emission lines while Type 2 objects show only narrow lines. There is a continuum of objects in between (intermediate types), where the broad line components are increasingly difficult to be observed.

Despite the huge radiative power of AGN, obscuration represents an important challenge for uncovering their complete pop-

ulation and explaining the complicated mechanisms that regulate these systems (Hickox & Alexander 2018). Regarding the different obscuring material, X-ray energies are obscured by gas whereas UV/optical/IR are extinguished by dust. A reliable method to identify and quantify obscuration is through X-ray observations. Modelling of the X-ray spectrum provides a robust estimation of the N_{H} column density.

The combination of optical and IR data provides us, also, with a powerful tool to search for obscured AGN. The optical emission of the SMBH is attenuated by dust and is re-emitted in the near to mid-IR wavelengths. In this case the galaxy appears faint in the optical but bright in the IR (LaMassa et al. 2016). Various optical/IR colour criteria have been used in the literature to identify red AGN, using either *Spitzer* (e.g. Fiore et al. 2009; Hickox et al. 2007; LaMassa et al. 2016; Donoso et al. 2014) or WISE (Yan et al. 2013) IR bands.

Previous studies have found a correlation between the optical/IR colours and X-ray absorption (e.g. Civano et al. 2012). On the other hand, Koutoulidis et al. (2018) found that reddened AGN are equally divided into X-ray absorbed and unabsorbed. Specifically, they used about 1500 X-ray AGN, from five deep *Chandra* fields (CDF-N, CDF-S, ECDF-S, COSMOS, AEGIS), and divided them into obscured and unobscured sources using X-ray (Hardness Ratio) and optical/mid-IR criteria ($R-[4.5] = 6.1$). Nevertheless their sources span low luminosities ($10^{42} - 10^{43}$ ergs $^{-1}$). Based on their findings they suggested that host galaxy contamination in the mid-IR bands affects the optical/mid-IR AGN classification.

We examine whether red AGN are also absorbed in X-rays. To this aim, we use X-ray AGN in the *XXL* survey (Pierre et al. 2016, hereafter *XXL* paper I) and select IR AGN candidates, by applying the criteria of Assef et al. (2018). We use optical/MIR colours (Yan et al. 2013) to select optically red sources. The final sample is restricted to those AGN that have also available X-ray spectroscopy (47 sources). In section 3.1 we fit the X-ray spectra to quantify the X-ray absorption of the sources. In addition we construct Spectral Energy Distributions (SED) using optical, near-IR and MIR photometry. We use the CIGALE code (Ciesla et al. 2015) to fit the SEDs and get an estimation of various absorption indices (AGN emission, torus inclination). We also complement our analysis with available optical spectra (see section 3.3). Finally, we compare the results of different wavelength/techniques for each red AGN.

2. Data

The data of this study come from the *XXL* survey. In this section we describe the survey as well as the sample selection.

2.1. XXL

The *XXL* survey is a medium-depth X-ray survey that covers a total area of 50 deg 2 . It covers two fields of nearly equal size, the *XXL* North (*XXL* – N) and the *XXL* South (*XXL* – S). Furthermore, it is the largest XMM-Newton project approved to date (>6 Msec) with median exposure at 10.4 ks and depth $\sim 6 \times 10^{-15}$ erg sec $^{-1}$ cm $^{-2}$ for point source at the 90% completeness limit in the [0.5-2] keV band (*XXL* paper I). In this study, we use the *XXL* – N sample that consists of 14 168 sources, including extended objects. To identify the X-ray detections at other wavelengths the X-ray counterparts have been crossmatched with optical, near-IR and mid-IR surveys (for more details see Chiappetti et al. 2018, hereafter *XXL* paper XXVII).

2.2. IR AGN candidates

WISE (Wright et al. 2010) completed an all-sky coverage in four mid-IR bands: 3.4, 4.6, 12 and 22 μm (W1, W2, W3 and W4 bands, respectively). Various colour criteria used these IR bands to, efficiently, identify AGN candidates. For instance, Mateos et al. (2012) suggested a selection method using three WISE colours. Stern et al. (2012) used the W1 and W2 bands and applied the following criterion: $W1 - W2 \geq 0.8$ to select AGN with $W2 < 15.05$ in the COSMOS field. Assef et al. (2013) extended the latter criterion and provided a selection of AGN for fainter WISE sources, using the WISE All-Sky data release catalogue. Assef et al. (2018) modified these criteria to incorporate data obtained during the post-cryogenic main mission extension (AllWISE catalogue).

In this study, we use $\sim 500\,000$ WISE detections included in the latest WISE catalogue (AllWISE) that lie within the XMM-XXL area to select IR AGN candidates, by applying the criteria of Assef et al. (2018). Specifically, we use:

$$W1 - W2 \geq \alpha_R, \quad W2 \leq \gamma_R \quad (1)$$

$$W1 - W2 > \alpha_R \exp [\beta_R (W2 - \gamma_R)^2], \quad W2 > \gamma_R \quad (2)$$

where, $(\alpha_R, \beta_R, \gamma_R) = (0.650, 0.153, 13.86)$, to select AGN at a 90% reliability.

2.3. Red AGN

To select optically red sources, among the IR AGN candidates, we apply the Yan et al. (2013) criterion ($r - W2 > 6$). This analysis reveals 561 red AGN. We cross-match this subsample with the *XXL* catalogue to identify the X-ray counterparts of these sources. For the cross-match, we use a radius of 3 arcsecs. Within this radius and given the X-ray source sky density, we find that a fraction of $\sim 0.2\%$ of spurious matches is expected (Mountrichas et al. 2017). To study the X-ray absorption of the optically red AGN population, we apply an X-ray spectral fitting analysis. As one of our main goals is to quantify the obscuration in the red AGN, we chose to analyse only the X-ray spectra of the sources with reliable photon statistics. For this reason, we keep only the sources with 50 net counts, or more, per detector (see Corral et al. 2015). There are 47 red AGN that meet the aforementioned X-ray criteria. Table 1 presents the number of sources in the various subsamples. Table 2 presents the ID along with the redshift and r, W2 magnitudes, in the Vega system, for the 47 optically red AGN.

Apart from the optical and mid-IR photometry, 45 out of 47 AGN have also been detected in the near-IR (VISTA; Emerson et al. 2006; Dalton et al. 2006). The *XXL* field has been observed by the SPIRE instrument onboard *Herschel* mission at far-IR wavelengths (Oliver et al. 2012). To identify the far-IR counterparts, we used the ARCHES cross-correlation tool XMATCH (Pineau et al. 2017). The details of the cross-match procedure are given in Section 2.2 of (Masoura et al. 2018). We find nine sources with *Herschel* photometry. Finally, 33/47 sources have available optical spectra. The vast majority of them (30 out of 33) come from the SDSS (DR15) survey. The remaining optical spectra are from the Galaxy And Mass Assembly (GAMA; Driver et al. 2011; Baldry et al. 2010) and the VIPERS (Guzzo et al. 2014; Scoville et al. 2018) surveys. In our analysis,

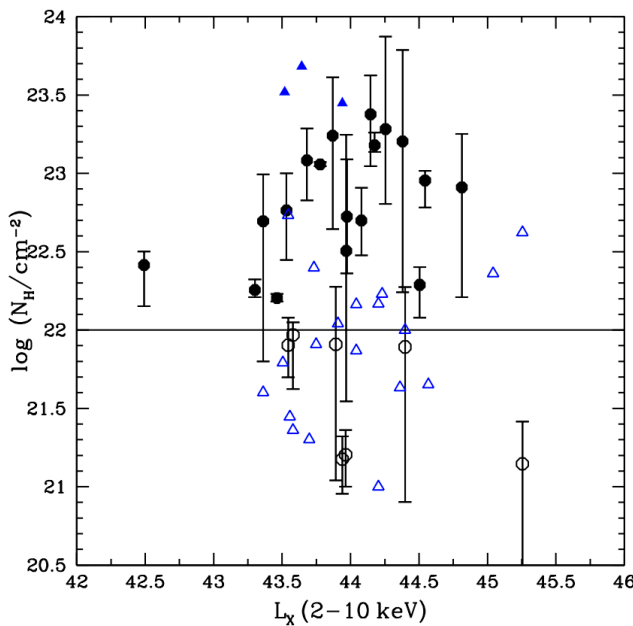


Fig. 1: The N_{H} as a function of X-ray luminosity for the 47 optical red AGN. Those sources that the X-ray spectral fitting could not constrain their N_{H} , are presented with a triangle (upper limit estimations). The 21 AGN that satisfy our X-ray absorption criteria are presented with filled symbols (see text for more details).

we use spectroscopic redshifts for 33 sources. For the remaining AGN we use their photometric redshifts, estimated in Fotopoulou et al. (2016) (hereafter XXL paper VI)]. The photometric redshift accuracy is 0.095 (for the full XMM-XXL catalogue). In our analysis, we incorporate the full Probability Density Function (PDF) of the photometric redshifts, when we calculate the uncertainties of the various parameters.

3. Analysis

We classify the 47 optically red AGN of our sample as obscured or unobscured using different criteria. Specifically, we examine their X-ray spectra, SEDs and optical spectra.

3.1. X-ray spectra

We examine the X-ray absorption of the 47 red AGN in our sample. To achieve that, we apply X-ray spectral-fitting using the XSPEC v12.10 software Arnaud (1996). We use Cash statistics (C-stat; Cash 1979) to the spectra binned to 1 count/bin, which has been proven to recover the actual spectral parameters in the most accurate way even for very low-count spectra (e.g., Krumpe et al. 2010). The model applied to the spectral data is a simple power law, $A(E) = KE^{-\Gamma}$, absorbed by both the Galactic photoelectric absorption as well as the intrinsic absorption. Γ is the photon index of the power-law and K is the flux at 1 keV in units of photons/keV/cm²/s. The Galactic absorption is taken from the Leiden/Argentine/Bonn (LAB) Survey of Galactic HI Kalberla et al. (2005). The X-ray spectra for the 47 AGN are presented in Figures A.1- A.47. The best-fit values are presented in Table 3. In Fig. 1 we present the N_{H} vs. the X-ray luminosity.

Fig. 2 presents the N_{H} distribution of the sources, taking into account the N_{H} upper limits (Isobe et al. 1986). For that purpose,

we use the Astronomical SURVival Statistics (ASURV; Lavalley et al. 1992) software package, that adopts the maximum-likelihood Kaplan-Meier estimator to take into account censored data (Feigelson & Nelson 1985). The derived mean value is $\log N_{\text{H}}/\text{cm}^{-2} = 21.80 \pm 0.13$. The distribution shows that the red sources are almost equally divided between obscured ($N_{\text{H}} > 10^{22}\text{cm}^{-2}$) and unobscured AGN. The limit of $N_{\text{H}} = 10^{22}\text{cm}^{-2}$ is often used in X-rays because lower column densities could be produced by dust lanes in the galaxy instead of the torus (Malkan et al. 1998). However, note that Merloni et al. (2013) proposes an alternative dividing line of $3 \times 10^{21}\text{cm}^{-2}$ in the sense that this provides a much better agreement when compared with the optical classification between type-1 and type-2 AGN. From Figures 1 and 2 it appears that the red r-W2 colour alone cannot guarantee that the source will be classified as obscured in X-rays.

3.2. SED fitting

We calculate the contribution of the AGN to the power output of the host galaxy, through the Code Investigating GALaxy Emission (CIGALE; Burgarella et al. 2005; Noll et al. 2009). We provide the CIGALE code version 2018.0 with multi-wavelength flux densities, using optical, near-IR and mid-IR photometry. Table 4 presents the models and the parameters used by CIGALE for the SED fitting of our X-ray sample. The Fritz et al. (2006) library of templates was used to model the AGN emission. The AGN fraction is measured as the AGN emission relative to infrared luminosity ($1 - 1000\mu\text{m}$). τ is the e-folding time of the main stellar population model in Myr. Age is defined as the age of the main stellar population in Myr. The extinction of a source is derived from the viewing angle, Ψ , of the torus. $\Psi \leq 30^\circ$ for Type 2 (edge-on), $40^\circ \leq \Psi = 60^\circ$ for intermediate and $\Psi \geq 70^\circ$ for Type 1 AGN (face-on; Ciesla et al. 2015), respectively. No intermediate values are used. The results from these fits appear in Table 7 and the SEDs are shown in Figures A.1- A.47 (for more details on the SED fitting see also Masoura et al. 2018).

As mentioned in the previous Section, nine of the sources in our sample have available Herschel photometry. We fit the SEDs of these sources with and without far-IR data to check whether the lack of far-IR photometric bands affects the SED fitting measurements. Specifically, we are interested on the inclination angle Ψ , since this parameter is used as a proxy to determine the obscuration of an AGN. We find that the inclusion of far-IR photometry in the SED fitting does not change the AGN emission nor the estimated inclination angle of the sources. Thus, we conclude that lack of far-IR photometry for the remaining of the sources, does not affect our analysis.

3.3. Optical Spectra

The optical spectra for 33 out of 47 sources are presented in Figures A.1- A.47. Optically unobscured sources (type 1) are considered to be those with broad emission lines (BL). Whereas obscured sources (type 2) exhibit only narrow emission lines (NL) or a red continuum. The AGN are characterised as obscured, unobscured or intermediate (IMD) type, based on their optical spectra, by visual inspection. Table 6 contains the classification according to the optical spectrum for each object.

To verify the redshift of our sources and assess their obscuration in the optical band we have used the optical spectra provided by the SDSS. We have recomputed the spectroscopic redshift and for a small number of cases we provide in Table 2 a different measurement from the one in SDSS.

Table 1: Number of IR selected AGN with X-ray/optical observations and spectra in the XMM-XXL field.

	Total number	X-ray Detections	X-ray Spectra
IR AGN	4798	1503	312
IR AGN with SDSS	2652	1268	262
Red AGN	561	135	47

Table 2: General properties of the red AGN sample.

Object	3XLSS ID	redshift	r (Vega)	W ₂ (Vega)
1	J021835.7-053758	0.387	19.84	13.56
2	J022848.4-044426	1.046	21.14	15.03
3	J022928.4-051124	0.307	17.76	11.65
4	J022809.0-041235	0.879	19.46	13.01
5	J020654.9-064552	1.412	21.12	14.82
6	J020410.4-063924	0.414	21.83	14.65
7	J023315.5-054747	0.598	20.91	13.70
8	J021337.9-042814	0.419	18.54	12.17
9	J020436.4-042833	0.827	19.77	13.46
10	J020543.0-051656	0.653	20.78	13.93
11	J020517.3-051024	0.792	21.05	14.92
12	J022244.3-030525	0.637	21.74	14.39
13	J022323.4-031157	0.691	20.42	13.90
14	J022209.6-025023	0.400	21.36	14.51
15	J022750.7-052232	0.804	22.26	13.98
16	J022758.4-053306	0.956	21.49	13.74
17	J022453.2-054050	0.488	20.76	13.32
18	J022258.8-055757	0.732	21.60	13.70
19	J021844.6-054054	0.671	21.19	13.88
20	J021523.2-044337	0.860	19.96	13.21
21	J022321.9-045739	0.779	21.34	13.83
22	J022443.6-050905	0.943	21.55	14.93
23	J023418.0-041833	0.582	22.57	15.07
24	J020543.7-063807	0.772	22.72	14.79
25	J022932.6-055438	1.263	19.70	13.53
26	J021239.2-054816	0.711	22.32	15.10
27	J021511.4-060805	0.772	22.34	14.19
28	J021808.8-055630	0.572	20.05	14.06
29	J022538.9-040821	0.733	21.28	14.68
30	J020845.1-051354	1.46	23.39	15.16
31	J020953.9-055102	0.642	20.91	14.11
32	J020806.6-055739	0.539	21.34	13.83
33	J021509.0-054305	0.70	22.48	14.53
34	J021512.9-060558	1.14	23.36	15.14
35	J020529.5-051100	1.20	23.40	14.94
36	J022404.0-035730	0.17	22.79	14.88
37	J023501.0-055234	0.85	22.49	15.06
38	J020210.6-041129	2.71	21.09	14.08
39	J022650.3-025752	1.21	22.79	14.63
40	J021303.7-040704	1.35	22.20	15.32
41	J023357.7-054819	1.60	24.20	14.69
42	J020335.0-064450	0.67	23.28	15.05
43	J020823.4-040652	2.23	24.68	14.92
44	J020135.4-050847	0.73	23.14	15.16
45	J021837.2-060654	0.943	21.47	15.11
46	J022149.9-045920	1.461	23.05	14.79
47	J020311.3-063534	1.05	22.96	15.19

Notes. r is the SDSS photometric band (SDSS DR15; Aguado et al. 2019). r and W₂ magnitudes are on the Vega system. We use three decimal points for spectroscopic redshifts and photometric redshifts are in italics with two decimal points.

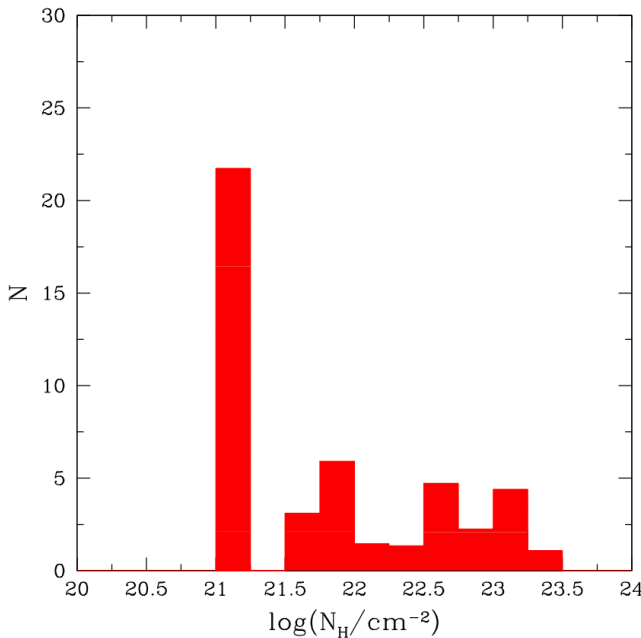


Fig. 2: N_{H} distribution taking into account N_{H} upper limits, for more details see text.

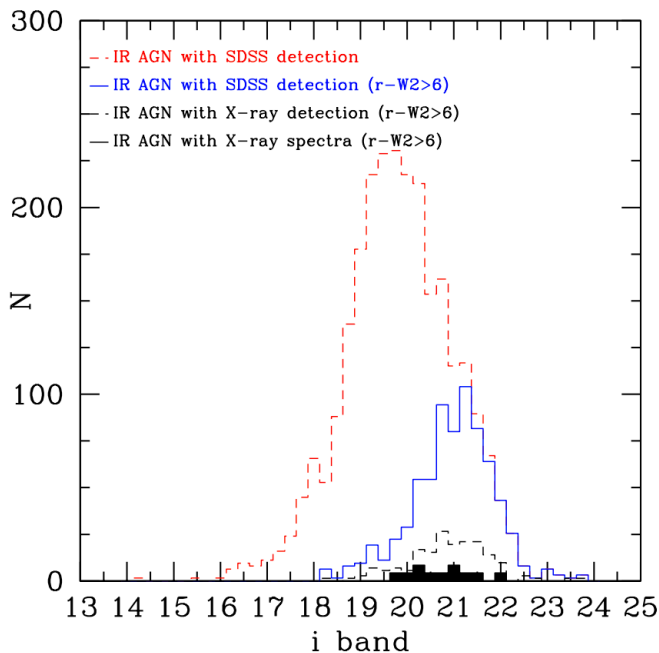


Fig. 3: i-band distribution of our sample. Red sources occupy the faint part of the i-band distribution

4. Discussion

Our IR selection criteria identify 4798 AGN candidates (Table 1). 2652 of them have been observed by SDSS. $\sim 20\%$ of these sources are optically red, using the criteria of Yan et al. (2013) (Table 1). Figures 3 and 4 show the i-band and the $r - W2$ distributions of the various samples. As expected, red sources occupy the faint part of the i-band distribution while the AGN sample with available X-ray spectra lacks sources with the highest $r - W2$ values.

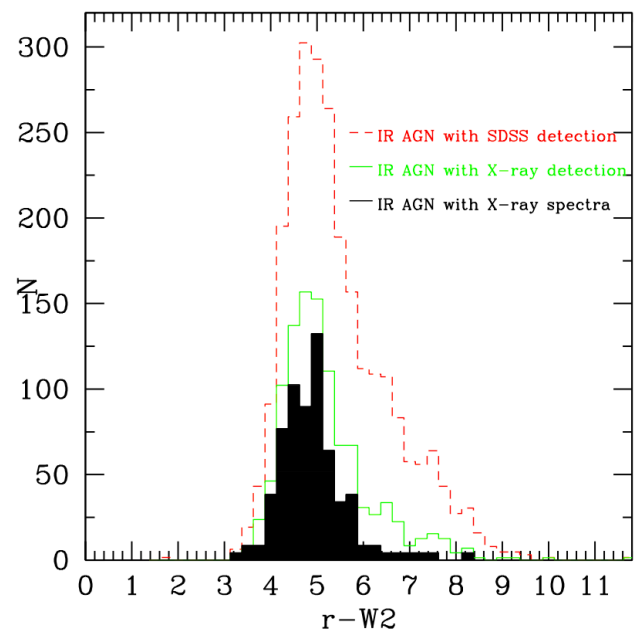


Fig. 4: $r - W2$ distribution of our sample. The AGN sample with available X-ray spectra lacks sources with the highest $r - W2$ values.

In our analysis, we explore the X-ray spectral properties of the 47 optically red AGN and examine whether these sources are also X-ray absorbed. Furthermore, we search for indications of extinction either on their SEDs or in their optical spectra. The results of the X-ray spectral fitting are presented in Table 3. For those cases where the photon index (Γ) is unphysically low ($\Gamma < 1.2$) we quote the N_{H} estimations with Γ fixed to $\Gamma = 1.8$ (Nandra & Pounds 1994). The latter N_{H} estimation is used to characterise the X-ray absorption of the source. Our analysis reveals 18 sources with best-fit intrinsic column densities $N_{\text{H}} > 10^{22} \text{ cm}^{-2}$. We also consider as possibly absorbed a source with upper limit that lies above the arbitrary chosen limit of $N_{\text{H}} = 10^{23} \text{ cm}^{-2}$ (i.e. J020543.0-051656, J020953.9-055102, J021509.0-054305). The latter increases the number of candidate X-ray absorbed sources to 21. We characterize these systems as X-ray absorbed sources and mark them in bold in Table 7. However, there are AGN that present mild absorption and could be classified as X-ray absorbed if we eased our X-ray criteria. Thus, lowering our X-ray absorption criteria, i.e., $N_{\text{H}} > 10^{21.5} \text{ cm}^{-2}$ (Merloni et al. 2013) or upper limit that lies above the N_{H} value $N_{\text{H}} = 10^{22} \text{ cm}^{-2}$, we find 13 additional sources that present signs of X-ray absorption. These additional sources are shown in italics in Table 7. Therefore, up to 34 AGN (72%) in the sample present some signs of X-ray absorption.

The vast majority of our optically red AGN have SEDs that show clear signs of obscuration in their AGN emission (green lines in Figures A.1-50). However, the AGN emission of the source J022809.0-041235 (no. 4 in Table 5) extends to the optical part of the spectrum without presenting signs of even mild obscuration. This source has also large Ψ ($\Psi = 80^\circ$) that also indicates a type 1 AGN (X-ray and optical spectra also confirm this is an unobscured AGN). There are two more sources with large Ψ value (i.e., observed face-on), specifically sources J020517.3-051024 and J021808.8-055630 (no. 11 and 28 in Table 5). Their SED reveals that even though the AGN emission extends to the

optical part of the SED, the emission of the galaxy is a dominant component of the SED at the optical wavelengths. We call the latter two systems galaxy dominated. We attribute this term to sources that satisfy the following criteria: (i) The IR (W2) emission of the system is due to the AGN emission and (ii) there is a strong galaxy emission in the optical part of the SED even though the AGN emission is only mildly obscured (or not obscured at all). Specifically, the ratio of the galaxy emission to the AGN emission in the r band is ≥ 1 . Although source no. 28 is not X-ray absorbed, source no. 11 presents signs of mild X-ray absorption ($N_H = 0.78^{+1.10}_{-0.70} \times 10^{22} \text{ cm}^{-2}$). The optical spectra of these two systems have broad emission lines, corroborating that these are unobscured sources. We conclude that the SEDs for 44 out of the 47 sources in our sample, present clear signs of obscuration, based on their AGN emission and their Ψ values.

Apart from these two AGN (i.e. sources 11 and 28 in Table 5), there are eight more sources that satisfy our aforementioned criteria and are therefore considered galaxy dominated systems (no. 5, 7, 10, 26, 35, 39, 44, 47). In these systems the galaxy/AGN emission in the r band ranges from ≈ 1 (e.g. no. 28) to ≥ 10 (e.g. 10, 39, 47). Five of these sources are among the AGN that are also X-ray absorbed (no 10, 26, 35, 39, 47 in Table 7). Their AGN fraction, $\text{frac}_{\text{AGN}} = 40 - 80\%$ (Table 5). These suggest that these systems are galaxy dominated because the AGN is obscured and not because the active SMBH is intrinsically weak. However, for the remaining three galaxy-dominated systems (no. 5, 7, 44), that are not X-ray absorbed, it could be that they are characterised as optically red ($r\text{-W2} > 6$) due to an intrinsically weak AGN (AGN fraction, $\text{frac}_{\text{AGN}} = 20 - 30\%$, Table 5) rather than an obscured AGN. Galaxy dominated systems are known to confuse optical/mid-IR criteria (Koutoulidis et al. 2018).

Excluding the ten galaxy dominated systems from our sample of red IR AGN, reduces the total number of red sources to 37. 17 (46% of the total sample) and 28 (76% of the total sample) of them are X-ray absorbed, using the strict and loose criteria, respectively. Therefore, there are nine ($\sim 20\%$) IR, red AGN in our sample, that present no signs of X-ray absorption. The optical spectra for two of these sources present narrow emission lines (no. 16, 20 in Table 7), four present broad emission lines (no. 1, 3, 9, 25 in Table 7) and two are of intermediate type (no. 17, 18 in Table 7), based on our visual inspection. The optical spectrum of source no. 23, is too noisy to extract any information. Previous studies have found that selection of obscured AGN based on optical/mid-IR colours are 80% reliable (Hickox et al. 2007). This could explain why, at least some of these nine AGN, although optically red present broad emission lines in their spectra and no substantial X-ray absorption.

Recently, Jaffarian & Gaskell (2020) studied the optical E(B-V) reddening vs. the X-ray absorbing column density for a large sample of Seyfert galaxies with both E(B-V) and X-ray absorption column density measurements. They find a significant correlation between E(B-V) and N_H albeit with a large scatter of $\pm \text{dex}$. They claim that this could be attributed to X-ray column density variability. Regardless the origin of the physical interpretation, the presence of such a large scatter can readily explain why some of our red sources show no signs of significant absorption in X-rays. The fact that the average absorbing column density derived for the red $r - W2 > 6$ sources is only $N_H = 21.8 \pm 0.13$ suggests that the above obscuration criterion selects sources with lower absorption compared to those selected in X-rays using $N_H > 10^{22} \text{ cm}^{-2}$ (e.g. Akylas et al. 2006; Ueda et al. 2014). In other words, the optically red source selection does not correspond to the same level of obscuring column den-

sities as those witnessed by X-rays. Hickox et al. (2017) have proposed an additional criterion for the selection of obscured AGN which is based on the combination of the u and WISE W3 band. Since there is not a unique definition of how obscured an AGN must be to be classified as absorbed, the various selection criteria target different ranges of obscuration. Specifically, the application of the usual X-ray criterion $N_H > 10^{22} \text{ cm}^{-2}$ selects the most obscured part of the obscured AGN distribution, while the $r\text{-W2}$ criterion extends to lower levels of obscuration. Finally, the Hickox et al. $u\text{-W3}$ criterion is sensitive to the lowest levels of obscuration. This is due to the use of the u band that is easily affected by even small amounts of reddening. Then, obviously, the different selection criteria result in different obscured AGN samples. This is most probably the reason why only 76%, at most, of the red AGN sample is absorbed in X-rays having column densities $\log N_H/\text{cm}^{-2} > 21.5$.

5. Summary

We applied the Assef et al. (2018) criteria based on the W1 and W2 WISE bands to select IR AGN in the XXL-North 25 deg^2 survey area. The above criteria yield 4798 AGN. Next, we applied the optical mid-IR colour criterion $r\text{-W2}$ (Yan et al. 2013) in order to select obscured AGN. We identified 561 red AGN of which 135 are detected in X-rays while 47 have good photon statistics (at least 50 net counts per detector) so that a reliable estimate of the absorbing column density can be derived. We used XSPEC to fit the X-ray spectra of the 47 sources and quantify their X-ray absorption. 76% of our sources may show signs of absorption higher than $\log N_H/\text{cm}^{-2} = 21.5$. Furthermore, we applied the CIGALE code in order to study the SEDs of our 47 red sources. The SED analysis revealed that 10/47 sources are galaxy dominated systems as the red colours are attributed to the host galaxy rather than absorption. In the vast majority of the remaining 37 sources, the SEDs confirm the presence of significant obscuration. The exact nature of the red sources which show low levels of X-ray absorption (25%) in apparent contradiction with their SEDs is unclear. A large scatter in the $r\text{-W2}$ colours vs. column density because of variability of the column density may offer a likely explanation. Our work shows that the $r\text{-W2}$ selection provides a robust method for selecting obscured AGN. However, it may identify also sources which present lower levels of obscuration when compared with the widely used X-ray spectroscopic criteria which usually define obscured sources as those having $\log N_H/\text{cm}^{-2} > 21.5$.

Acknowledgements. The authors are grateful to the anonymous referee for helpful comments. VAM and GM acknowledge support of this work by the PROTEAS II project (MIS 5002515), which is implemented under the "Reinforcement of the Research and Innovation Infrastructure" action, funded by the "Competitiveness, Entrepreneurship and Innovation" operational programme (NSRF 2014-2020) and co-financed by Greece and the European Union (European Regional Development Fund). GM also acknowledges support by the Agencia Estatal de Investigación, Unidad de Excelencia María de Maeztu, ref. MDM-2017-0765. The Saclay group acknowledges long-term support from the Centre National d'Etudes Spatiales (CNES).

XXL is an international project based around an *XXM* Very Large Programme surveying two 25 deg^2 extragalactic fields at a depth of $\sim 6 \times 10^{-15} \text{ erg cm}^{-2} \text{ s}^{-1}$ in the [0.5-2] keV band for point-like sources. The XXL website is <http://irfu.cea.fr/xxl/>. Multi-band information and spectroscopic follow-up of the X-ray sources are obtained through a number of survey programmes, summarised at <http://xxlmultiwave.pbworks.com/>.

This research has made use of data obtained from the 3XMM XMM-Newton serendipitous source catalogue compiled by the 10 institutes of the XMM-Newton Survey Science Centre selected by ESA.

The Saclay group acknowledges long-term support from the Centre National d'Etudes Spatiales (CNES).

This work is based on observations made with XMM-*Newton*, an ESA science mission with instruments and contributions directly funded by ESA Member States and NASA.

Funding for the Sloan Digital Sky Survey IV has been provided by the Alfred P. Sloan Foundation, the U.S. Department of Energy Office of Science, and the Participating Institutions. SDSS-IV acknowledges support and resources from the Center for High-Performance Computing at the University of Utah. The SDSS web site is www.sdss.org.

SDSS-IV is managed by the Astrophysical Research Consortium for the Participating Institutions of the SDSS Collaboration including the Brazilian Participation Group, the Carnegie Institution for Science, Carnegie Mellon University, the Chilean Participation Group, the French Participation Group, Harvard-Smithsonian Center for Astrophysics, Instituto de Astrofísica de Canarias, The Johns Hopkins University, Kavli Institute for the Physics and Mathematics of the Universe (IPMU) / University of Tokyo, Lawrence Berkeley National Laboratory, Leibniz Institut für Astrophysik Potsdam (AIP), Max-Planck-Institut für Astronomie (MPIA Heidelberg), Max-Planck-Institut für Astrophysik (MPA Garching), Max-Planck-Institut für Extraterrestrische Physik (MPE), National Astronomical Observatories of China, New Mexico State University, New York University, University of Notre Dame, Observatório Nacional / MCTI, The Ohio State University, Pennsylvania State University, Shanghai Astronomical Observatory, United Kingdom Participation Group, Universidad Nacional Autónoma de México, University of Arizona, University of Colorado Boulder, University of Oxford, University of Portsmouth, University of Utah, University of Virginia, University of Washington, University of Wisconsin, Vanderbilt University, and Yale University.

This publication makes use of data products from the Wide-field Infrared Survey Explorer, which is a joint project of the University of California, Los Angeles, and the Jet Propulsion Laboratory/California Institute of Technology, funded by the National Aeronautics and Space Administration.

The VISTA Data Flow System pipeline processing and science archive are described in Irwin et al. (2004), Hambly et al. (2008) and Cross et al. (2012). Based on observations obtained as part of the VISTA Hemisphere Survey, ESO Program, 179.A-2010 (PI: McMahon). We have used data from the 3rd data release.

- Jaffarian, G. W. & Gaskell, C. M. 2020, MNRAS [<https://arxiv.org/abs/2001.08900v1>]
- Kalberla, P. M. W., Burton, W. B., Hartmann, D., et al. 2005, A&A, 440, 775
- Kormendy, J., Bender, R., Ajhar, E. A., et al. 1996a, ApJ, 473, L91
- Kormendy, J., Bender, R., Richstone, D., et al. 1996b, ApJ, 459
- Koutoulidis, L., Georgantopoulos, I., Mountrichas, G., et al. 2018, MNRAS, 481, 3063
- Krumpe, M., Miyaji, T., & Coil, A. L. 2010, ApJ, 713, 558
- LaMassa, S. M., Civano, F., Brusa, M., et al. 2016, ApJ, 818, 88
- Lavalley, M., Isobe, T., & Feigelson, E. 1992, in Astronomical Society of the Pacific Conference Series, Vol. 25, Astronomical Data Analysis Software and Systems I, ed. D. M. Worrall, C. Biemesderfer, & J. Barnes, 245
- Malkan, M. A., Gorjian, V., & Tam, R. 1998, Astrophys. J., Suppl. Ser., 117, 25
- Masoura, V. A., Mountrichas, G., Georgantopoulos, I., et al. 2018, A&A, 618, A31
- Mateos, S., Alonso-Herrero, A., Carrera, F. J., et al. 2012, MNRAS, 426, 3271
- Merloni, A., Bongiorno, A., Brusa, M., et al. 2013, MNRAS, 437, 3550
- Mountrichas, G., Georgantopoulos, I., Secret, N. J., et al. 2017, MNRAS, 468, 3042
- Nandra, K. & Pounds, K. A. 1994, MNRAS, 268, 405
- Nenkova, M., Siroky, M. M., Nikutta, R., Ivezić, Ž., & Elitzur, M. 2008a, ApJ, 685, 160
- Nenkova, M., Siroky, M. M.; Ivezić, Ž., & Elitzur, M. 2008b, ApJ, 685, 147
- Netzer, H. 2015, ARA&A, 53, 365
- Noll, S., Burgarella, D., Giovannoli, E., et al. 2009, A&A, 507, 1793
- Oliver, S. J. et al. 2012, MNRAS, 424, 1614
- Pierre, M., Pacaud, F., Adamo, C., et al. 2016, A&A, 592, A1
- Pineau, F.-X., Derriere, S., Motch, C., et al. 2017, A&A, 597, A89
- Scodéglio, M., Guzzo, L., Garilli, B., et al. 2018, A&A, 609, A84
- Siebenmorgen, R., Heymann, F., & Efstathiou, A. 2015, A&A, 583, A120
- Stalevski, M., Ricci, C., Ueda, Y., et al. 2016, MNRAS, 458, 2288
- Stern, D., Assef, R. J., Benford, D. J., et al. 2012, ApJ, 753, 30
- Ueda, Y., Akiyama, M., Hasinger, G., Miyaji, T., & Watson, M. G. 2014, ApJ, 786, 104
- Ulrich, M.-H., Maraschi, L., & Urry, C. M. 1997, ARA&A, 35, 445
- Wilkins, D. R. & Gallo, L. C. 2015, MNRAS, 448, 703
- Wright, E. L., Eisenhardt, P. R. M., Mainzer, A. K., et al. 2010, AJ, 140, 1868
- Yan, L., Donoso, E., Tsai, C.-W., et al. 2013, AJ, 145, 55

References

- Aguado, D. S., Hernández, J. I. G., Prieto, C. A., & Rebolo, R. 2019, ApJ, 874, L21
- Akylas, A., Georgantopoulos, I., Georgakakis, A., Kitsionas, S., & Hatziminaoglou, E. 2006, A&A, 459, 693
- Antonucci, R. 1993, ARA&A, 31, 473
- Arnaud, K. A. 1996, ASPC, 101, 17
- Assef, R. J., Stern, D., Kochanek, C. S., et al. 2013, ApJ, 772, 26
- Assef, R. J., Stern, D., Noirot, G., et al. 2018, ApJS, 234, 23
- Baldry, I. K., Robotham, A. S. G., Hill, D. T., et al. 2010, MNRAS, 404, 86
- Burgarella, D., Buat, V., & Iglesias-Páramo, J. 2005, MNRAS, 360, 1413
- Calzetti, D., Armus, L., Bohlin, R. C., et al. 2000, ApJ, 533, 682
- Cash, W. 1979, ApJ, 228, 939
- Chiappetti, L., Fotopoulou, S., Lidman, C., et al. 2018, A&A, 620, A12
- Ciesla, L., Charmandaris, V., Georgakakis, A., et al. 2015, A&A, 576, A10
- Civano, F., Elvis, M., Brusa, M., et al. 2012, ApJS, 201, 30
- Corral, A., Georgantopoulos, I., Watson, M. G., et al. 2015, A&A, 576, A61
- Cross, N. J. G., Collins, R. S., Mann, R. G., et al. 2012, A&A, 548, A119
- Dalton, G. B., Caldwell, M., Ward, A. K., et al. 2006, SPIE, 6269
- Donoso, E., Yan, L., Stern, D., & Assef, R. J. 2014, ApJ, 789, 44
- Driver, S. P., Hill, D. T., Kelvin, L. S., et al. 2011, MNRAS, 413, 971
- Edelson, R. A. & Malkan, M. A. 1986, ApJ, 308, 59
- Emerson, J., McPherson, A., & Sutherland, W. 2006, Msngr, 126, 41
- Feigelson, E. D. & Nelson, P. I. 1985, ApJ, 293, 192
- Fiore, F., Puccetti, S., Brusa, M., et al. 2009, ApJ, 693, 447
- Fotopoulou, S., Pacaud, F., Paltani, S., et al. 2016, A&A, 592, A5
- Fritz, J., Franceschini, A., & Hatziminaoglou, E. 2006, MNRAS, 166, 767
- Guzzo, L., Scodéglio, M., Garilli, B., et al. 2014, A&A, 566, A108
- Haardt, F. & Maraschi, L. 1991, ApJ, 380, L51
- Hambly, N. C., Collins, R. S., Cross, N. J. G., et al. 2008, MNRAS, 384, 637
- Hickox, R. & Alexander, D. 2018, ARAA, 56, 625
- Hickox, R. C., Jones, C., Forman, W. R., et al. 2007, ApJ, 671, 1365
- Hickox, R. C., Myers, A. D., Greene, J. E., et al. 2017, ApJ, 849, 53
- Hönig, S. F. & Kishimoto, M. 2010, A&A, 523, A27
- Hönig, S. F. & Kishimoto, M. 2017, ApJ, 838, L20
- Hönig, S. F., Kishimoto, M., Gandhi, P., et al. 2010, A&A, 515, A23
- Irwin, M. J., Lewis, J., Hodgkin, S., et al. 2004, in Optimizing Scientific Return for Astronomy through Information Technologies (SPIE)
- Isobe, T., Feigelson, E. D., & Nelson, P. I. 1986, ApJ, 306, 490

Table 3: X-ray properties of the red AGN sample.

Object	3XLSS ID	$N_{\text{H}} \times 10^{22} \text{cm}^{-2}$	$N_{\text{H}} \times 10^{22} \text{cm}^{-2}$ $\Gamma = 1.8$	Γ	$\log L_{\text{X}}(2 - 10 \text{ keV})$ erg s^{-1}	C-stat/d.f.
1	J021835.7-053758	$0.15^{+0.06}_{-0.06}$	-	$1.85^{+0.15}_{-0.15}$	8.7×10^{43}	802/1027
2	<i>J022848.4-044426</i>	< 1.46	-	$1.77^{+1.40}_{-0.60}$	1.1×10^{44}	33/38
3	J022928.4-051124	$1.60^{+0.10}_{-0.08}$	-	$2.24^{+1.20}_{-0.30}$	2.9×10^{43}	512/578
4	J022809.0-041235	$0.14^{+0.12}_{-0.11}$	-	$1.87^{+0.21}_{-0.20}$	1.8×10^{45}	488/577
5	J020654.9-064552	< 0.23	-	$1.75^{+0.26}_{-0.25}$	3.8×10^{43}	103/155
6	<i>J020410.4-063924</i>	$0.81^{+0.89}_{-0.68}$	-	$1.86^{+0.70}_{-0.58}$	7.8×10^{43}	106/138
7	J023315.5-054747	< 0.62	-	$1.94^{+0.70}_{-0.40}$	3.2×10^{43}	89/107
8	J021337.9-042814	$12.1^{+7.20}_{-5.37}$	-	$1.60^{+0.60}_{-0.39}$	4.8×10^{43}	63/70
9	J020436.4-042833	< 0.45	-	$1.86^{+0.25}_{-0.24}$	3.7×10^{44}	510/550
10	J020543.0-051656	< 48.0	-	$1.80^{+8.10}_{-1.50}$	4.4×10^{43}	17/18
11	<i>J020517.3-051024</i>	$0.78^{+1.10}_{-0.70}$	-	$1.24^{+3.10}_{-0.90}$	2.5×10^{44}	22/46
12	J022244.3-030525	$23.8^{+18.30}_{-12.70}$	-	$1.51^{+1.20}_{-1.0}$	1.4×10^{44}	112/117
13	J022323.4-031157	$17.4^{+23.60}_{-13.00}$	-	$2.70^{+0.40}_{-0.20}$	7.4×10^{43}	27/39
14	<i>J022209.6-025023</i>	$0.80^{+0.40}_{-0.30}$	-	$1.90^{+0.40}_{-0.30}$	3.5×10^{43}	211/270
15	J022750.7-052232	$5.00^{+3.10}_{-2.00}$	-	$2.40^{+0.80}_{-0.70}$	1.2×10^{44}	154/179
16	J022758.4-053306	< 0.10	-	$1.40^{+0.90}_{-0.50}$	1.6×10^{44}	33/44
17	J022453.2-054050	$5.80^{+4.20}_{-3.00}$	-	$1.40^{+0.70}_{-0.20}$	3.4×10^{43}	56/66
18	J022258.8-055757	< 0.20	-	$1.60^{+2.60}_{-0.90}$	5.0×10^{43}	65/69
19	J021844.6-054054	< 0.74	-	$1.80^{+0.70}_{-0.40}$	1.1×10^{44}	146/157
20	J021523.2-044337	< 0.28	-	$2.10^{+0.80}_{-0.20}$	3.6×10^{43}	130/141
21	J022321.9-045739	$15.10^{+3.1}_{-1.40}$	-	$1.67^{+2.80}_{-1.80}$	1.5×10^{44}	93/92
22	<i>J022443.6-050905</i>	< 1.10	-	$1.33^{+0.48}_{-0.35}$	8.1×10^{43}	142/172
23	J023418.0-041833	< 0.40	-	$1.84^{+0.36}_{-0.45}$	2.3×10^{43}	15/16
24	J020543.7-063807	< 3.90	$8.1^{+2.2}_{-5.0}$	$1.18^{+0.54}_{-0.36}$	6.5×10^{44}	135/145
25	J022932.6-055438	< 0.43	-	$1.50^{+0.50}_{-0.40}$	2.3×10^{44}	62/82
26	J021239.2-054816	$11.40^{+0.30}_{-0.20}$	-	$1.80^{+0.60}_{-0.20}$	6.0×10^{43}	10/11
27	J021511.4-060805	< 22	$16.0^{+3.8}_{-9.2}$	$1.00^{+1.80}_{-1.50}$	2.4×10^{44}	48/50
28	J021808.8-055630	$0.16^{+0.07}_{-0.06}$	-	$1.98^{+0.22}_{-0.24}$	9.2×10^{43}	92/104
29	J022538.9-040821	$4.95^{+4.80}_{-4.30}$	-	$1.60^{+0.80}_{-0.30}$	2.3×10^{43}	31/34
30	<i>J020845.1-051354</i>	< 1.00	-	$1.90^{+0.70}_{-0.40}$	2.5×10^{44}	73/89
31	J020953.9-055102	< 28	-	$1.60^{+0.6}_{-0.8}$	8.7×10^{43}	37/30
32	J020806.6-055739	$1.80^{+0.30}_{-0.18}$	-	$2.30^{+1.20}_{-0.40}$	2.0×10^{43}	80/56
33	J021509.0-054305	< 33.00	-	$1.33^{+3.10}_{-1.90}$	3.3×10^{43}	30/28
34	<i>J021512.9-060558</i>	< 1.70	-	$1.71^{+0.70}_{-0.50}$	1.7×10^{44}	103/123
35	<i>J020529.5-051100</i>	< 1.47	-	$1.35^{+0.80}_{-0.40}$	1.6×10^{44}	86/90
36	J022404.0-035730	$5.30^{+7.15}_{-3.09}$	-	$1.82^{+0.40}_{-0.70}$	9.3×10^{43}	52/59
37	<i>J023501.0-055234</i>	< 5.40	-	$1.42^{+0.30}_{-0.60}$	3.5×10^{43}	33/23
38	<i>J020210.6-041129</i>	< 4.20	-	$1.22^{+0.90}_{-0.40}$	1.8×10^{45}	8/12
39	J022650.3-025752	$9.00^{+1.37}_{-2.94}$	-	$1.83^{+0.8}_{-0.4}$	3.5×10^{44}	56/70
40	J021303.7-040704	< 14.0	$19.2^{+3.9}_{-3.0}$	$0.70^{+1.10}_{-0.80}$	1.8×10^{44}	32/46
41	<i>J023357.7-054819</i>	< 2.30	-	$1.60^{+0.40}_{-0.40}$	1.1×10^{45}	192/259
42	<i>J020335.0-064450</i>	< 2.50	-	$1.50^{+1.38}_{-0.42}$	5.4×10^{43}	44/57
43	J020823.4-040652	< 0.50	$1.9^{+0.6}_{-1.6}$	$1.20^{+1.00}_{-0.70}$	3.2×10^{44}	55/58
44	J020135.4-050847	< 0.81	-	$1.35^{+0.80}_{-0.30}$	5.6×10^{43}	86/90
45	<i>J021837.2-060654</i>	$0.93^{+0.05}_{-0.28}$	-	$2.00^{+0.40}_{-0.30}$	3.8×10^{43}	158/172
46	J022149.9-045920	< 1.70	$2.6^{+0.5}_{-1.2}$	$1.10^{+1.30}_{-0.80}$	3.1×10^{42}	40/49
47	J020311.3-063534	$3.20^{+14.42}_{-2.85}$	-	$1.60^{+1.30}_{-0.90}$	9.3×10^{43}	20/30

Notes. When $\Gamma \leq 1.2$, then we quote the N_{H} estimations with Γ fixed to $\Gamma = 1.8$ and present the N_{H} estimations in column 4. Sources classified as X-ray obscured, based on our strict criteria (see text for more details), are presented in bold. Sources that satisfy the loosen X-ray criteria (see text) are shown in italics. The energy band of L_{X} is [2-10keV].

Table 4: The models and the values for their free parameters used by CIGALE for the SED fitting of our X-ray samples.

Parameter	Model/values
stellar population synthesis model	
initial mass function	Salpeter
metallicity	0.02 (Solar)
single stellar population library	Bruzual & Charlot (2003)
double exponentially decreasing (2τ dec) model	
τ	100, 1000, 5000, 10000
age	500, 2000, 5000, 10000, 12000
burst age	100, 200, 400
Dust extinction	
dust attenuation law	Calzetti et al. (2000)
reddening E(B-V)	0.01, 0.1, 0.3, 0.5, 0.8, 1.2
E(B-V) reduction factor between old and young stellar population	0.44
Fritz et al. (2006) model for AGN emission	
ratio between outer and inner dust torus radii	10, 60, 150
9.7 μ m equatorial optical depth	0.1, 0.3, 1.0, 2.0, 6.0, 10.0
β	-0.5
γ	0.0, 2.0, 6.0
Θ	100°
Ψ	0°, 10°, 20°, 30°, 40°, 50°, 60°, 70°, 80°, 90°
AGN fraction	0.1, 0.2, 0.3, 0.4, 0.5, 0.6, 0.7, 0.8, 0.9

Notes. τ is the e-folding time of the main stellar population model in Myr, age is defined as the age of the main stellar population in the galaxy in Myr, and burst age is the age of the late burst in Myr. β and γ are the parameters used to define the law for the spatial behaviour of density of the torus density. The functional form of the latter is $\rho(r, \theta) \propto r^\beta e^{-\gamma|\cos\theta|}$, where r and θ are the radial distance and the polar distance, respectively. Θ is the opening angle and Ψ the viewing angle of the torus. Type 2 AGN have $\Psi \leq 30^\circ$ (edge-on) and Type 1 AGN have $\Psi \geq 70^\circ$ (face-on). $40^\circ \leq \Psi \leq 60^\circ$ corresponds to intermediate type AGN. The AGN fraction is measured as the AGN emission relative to IR luminosity (1–1000 μ m).

Table 5: SED properties of the red AGN sample.

Object	3XLSS ID	Ψ (degrees)	frac _{AGN}	χ^2_{red}
1	J021835.7-053758	20	0.30 ^{+0.10} _{-0.10}	0.43
2	J022848.4-044426	40	0.30 ^{+0.10} _{-0.10}	6.35
3	J022928.4-051124	20	0.40 ^{+0.18} _{-0.10}	4.42
4	J022809.0-041235	80	0.30 ^{+0.15} _{-0.15}	1.52
5	J020654.9-064552	20	0.30 ^{+0.15} _{-0.15}	4.23
6	J020410.4-063924	40	0.50 ^{+0.15} _{-0.15}	2.99
7	J023315.5-054747	20	0.30 ^{+0.10} _{-0.10}	0.48
8	J021337.9-042814	10	0.60 ^{+0.05} _{-0.05}	2.50
9	J020436.4-042833	20	0.60 ^{+0.15} _{-0.15}	3.17
10	J020543.0-051656	20	0.50 ^{+0.05} _{-0.05}	0.47
11	J020517.3-051024	70	0.20 ^{+0.10} _{-0.10}	5.09
12	J022244.3-030525	40	0.40 ^{+0.15} _{-0.15}	0.43
13	J022323.4-031157	20	0.40 ^{+0.20} _{-0.20}	3.00
14	J022209.6-025023	30	0.30 ^{+0.15} _{-0.15}	2.71
15	J022750.7-052232	10	0.30 ^{+0.10} _{-0.10}	3.28
16	J022758.4-053306	0	0.60 ^{+0.05} _{-0.05}	3.13
17	J022453.2-054050	10	0.40 ^{+0.15} _{-0.15}	0.70
18	J022258.8-055757	20	0.50 ^{+0.05} _{-0.05}	2.72
19	J021844.6-054054	30	0.70 ^{+0.10} _{-0.10}	1.82
20	J021523.2-044337	30	0.50 ^{+0.15} _{-0.15}	3.04
21	J022321.9-045739	30	0.60 ^{+0.10} _{-0.10}	2.65
22	J022443.6-050905	10	0.30 ^{+0.10} _{-0.10}	0.56
23	J023418.0-041833	10	0.70 ^{+0.20} _{-0.20}	2.42
24	J020543.7-063807	40	0.60 ^{+0.10} _{-0.10}	0.13
25	J022932.6-055438	10	0.60 ^{+0.10} _{-0.10}	1.25
26	J021239.2-054816	50	0.80 ^{+0.20} _{-0.20}	3.34
27	J021511.4-060805	10	0.70 ^{+0.20} _{-0.20}	1.02
28	J021808.8-055630	80	0.30 ^{+0.10} _{-0.10}	2.30
29	J022538.9-040821	10	0.40 ^{+0.10} _{-0.10}	1.30
30	J020845.1-051354	50	0.30 ^{+0.10} _{-0.20}	1.28
31	J020953.9-055102	30	0.60 ^{+0.10} _{-0.10}	2.68
32	J020806.6-055739	40	0.60 ^{+0.10} _{-0.10}	0.92
33	J021509.0-054305	30	0.70 ^{+0.20} _{-0.20}	4.89
34	J021512.9-060558	0	0.80 ^{+0.10} _{-0.10}	0.18
35	J020529.5-051100	10	0.50 ^{+0.20} _{-0.20}	4.19
36	J022404.0-035730	20	0.30 ^{+0.20} _{-0.20}	0.60
37	J023501.0-055234	10	0.30 ^{+0.10} _{-0.20}	0.37
38	J020210.6-041129	10	0.30 ^{+0.05} _{-0.05}	1.46
39	J022650.3-025752	40	0.50 ^{+0.20} _{-0.20}	1.67
40	J021303.7-040704	30	0.80 ^{+0.10} _{-0.10}	0.19
41	J023357.7-054819	10	0.70 ^{+0.10} _{-0.20}	0.62
42	J020335.0-064450	10	0.70 ^{+0.20} _{-0.20}	0.03
43	J020823.4-040652	10	0.80 ^{+0.10} _{-0.20}	0.53
44	J020135.4-050847	20	0.20 ^{+0.20} _{-0.10}	0.62
45	J021837.2-060654	20	0.40 ^{+0.20} _{-0.20}	1.00
46	J022149.9-045920	30	0.80 ^{+0.10} _{-0.19}	0.36
47	J020311.3-063534	10	0.40 ^{+0.15} _{-0.15}	0.16

Notes. We consider sources with $\Psi \leq 30^\circ$ as Type 2 (edge-on), $40^\circ \leq \Psi \leq 60^\circ$ as intermediate and $\Psi \geq 70^\circ$ as Type 1 AGN, based on their best-fit values.

Table 6: Optical properties of the red AGN sample.

Object	3XLSS ID	Optical
1	J021835.7-053758	BL
2	J022848.4-044426	BL, flat
3	J022928.4-051124	BL
4	J022809.0-041235	BL, flat
5	J020654.9-064552	NL
6	J020410.4-063924	NL
7	J023315.5-054747	NL
8	J021337.9-042814	BL, blue
9	J020436.4-042833	BL
10	J020543.0-051656	BL
11	J020517.3-051024	BL
12	J022244.3-030525	NL, red
13	J022323.4-031157	IMD
14	J022209.6-025023	NL
15	J022750.7-052232	IMD
16	J022758.4-053306	NL
17	J022453.2-054050	IMD
18	J022258.8-055757	IMD
19	J021844.6-054054	IMD
20	J021523.2-044337	NL
21	J022321.9-045739	NL
22	J022443.6-050905	IMD
23	J023418.0-041833	noisy
24	J020543.7-063807	noisy
25	J022932.6-055438	BL
26	J021239.2-054816	noisy
27	J021511.4-060805	NL
28	J021808.8-055630	BL
29	J022538.9-040821	BL
30	J020845.1-051354	-
31	J020953.9-055102	BL
32	J020806.6-055739	NL, red
33	J021509.0-054305	-
34	J021512.9-060558	-
35	J020529.5-051100	-
36	J022404.0-035730	-
37	J023501.0-055234	-
38	J020210.6-041129	-
39	J022650.3-025752	-
40	J021303.7-040704	-
41	J023357.7-054819	-
42	J020335.0-064450	-
43	J020823.4-040652	-
44	J020135.4-050847	-
45	J021837.2-060654	noisy
46	J022149.9-045920	BL
47	J020311.3-063534	-

Notes. Optically unobscured sources (type 1) are considered to be those with broad emission lines (BL). Whereas obscured sources (type 2) exhibit only narrow emission lines (NL) or a red continuum. The AGN are characterised as obscured, unobscured or intermediate type (IMD), based on their optical spectra, by visual inspection. We note that in the optical spectra of sources no. 13 and 22, while the MgII lines are broad, all other lines are narrow lines. This is attributed to the wider area the the MgII originates from with respect to the Balmer lines. These sources, are characterized as IMD.

Table 7: Comparison of the X-ray, SED and optical properties.

Object	ID 3XLSS	Classification		
		Xray	SED	optical
1	J021835.7-053758	1	2	1
2	<i>J022848.4-044426</i>	2	2	1
3	J022928.4-051124	2	2	1
4	J022809.0-041235	1	1	1
5	J020654.9-064552	1	2	2
6	<i>J020410.4-063924</i>	2	2	2
7	J023315.5-054747	1	2	2
8	J021337.9-042814	2	2	1
9	J020436.4-042833	1	2	1
10	J020543.0-051656	2	2	1
11	<i>J020517.3-051024</i>	2	1	1
12	J022244.3-030525	2	2	2
13	J022323.4-031157	2	2	3
14	<i>J022209.6-025023</i>	2	2	2
15	J022750.7-052232	2	2	3
16	J022758.4-053306	1	2	2
17	J022453.2-054050	2	2	3
18	J022258.8-055757	1	2	3
19	J021844.6-054054	1	2	3
20	J021523.2-044337	1	2	2
21	J022321.9-045739	2	2	2
22	<i>J022443.6-050905</i>	2	2	3
23	J023418.0-041833	1	2	0
24	J020543.7-063807	2	2	0
25	J022932.6-055438	1	2	1
26	J021239.2-054816	2	2	0
27	J021511.4-060805	2	2	1
28	J021808.8-055630	1	1	1
29	J022538.9-040821	2	2	1
30	<i>J020845.1-051354</i>	2	2	-
31	J020953.9-055102	2	2	1
32	J020806.6-055739	2	2	2
33	J021509.0-054305	2	2	-
34	<i>J021512.9-060558</i>	2	2	-
35	<i>J020529.5-051100</i>	2	2	-
36	J022404.0-035730	2	2	-
37	<i>J023501.0-055234</i>	2	2	-
38	<i>J020210.6-041129</i>	2	2	-
39	J022650.3-025752	2	2	-
40	J021303.7-040704	2	2	-
41	<i>J023357.7-054819</i>	2	2	-
42	<i>J020335.0-064450</i>	2	2	-
43	J020823.4-040652	2	2	-
44	J020135.4-050847	1	2	-
45	<i>J021837.2-060654</i>	2	2	0
46	J022149.9-045920	2	2	2
47	J020311.3-063534	2	2	-

Notes. Sources classified as X-ray obscured, based on our strict criteria (see text for more details), are presented in bold. Sources that satisfy the loosen X-ray criteria (see text) are shown in italics. Numbers 1 (unobscured) and 2 (obscured) are used to denote the classification of the sources based on the various criteria. Numbers 0 and 3 refer to optical spectra that are too noisy to allow us to classify them and are IMD type, respectively. The first number refers to the X-ray classification, while the second and the third numbers correspond to the SED- and optical-based characterisation.

Appendix A: X-ray, optical spectra and SEDs

In this Section, we present the X-ray, SEDs and the optical spectra (when available) for each one of the 47 optically red sources in our sample. Numbers 1 and 2 are used to denote the classification of the sources based on the various criteria. Specifically, 1 refers to unobscured and 2 to obscured sources. Number 0 is used in those cases that the optical spectrum is too noisy to extract any useful information. Number 3 is used to denote IMD type of classification. The numbers in parentheses refer to the classification based on the X-ray spectrum, the SED and the optical spectrum, respectively. We use three decimal points for spectroscopic redshifts and two decimal points for photometric redshifts.

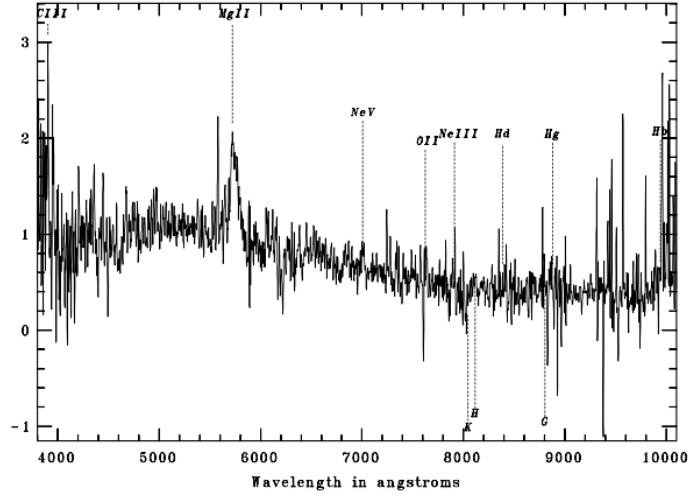
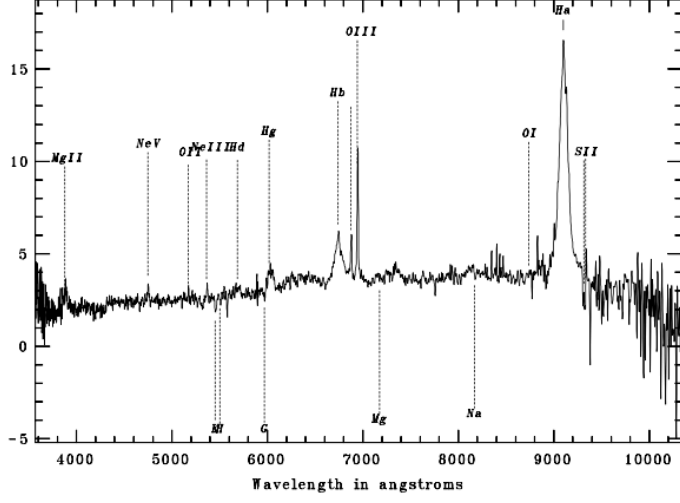
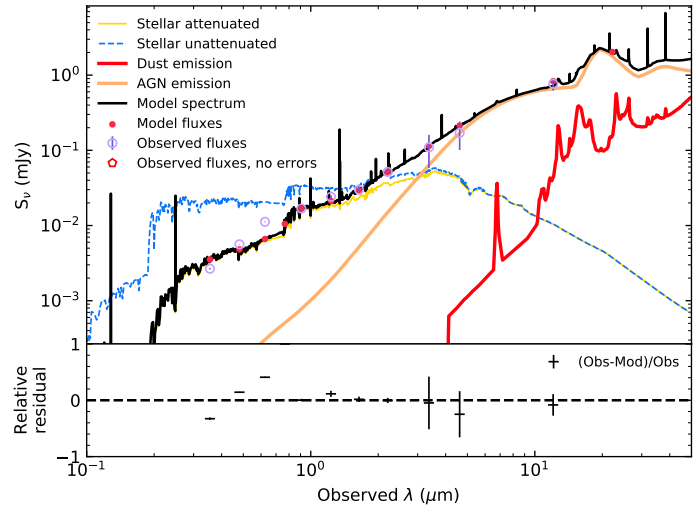
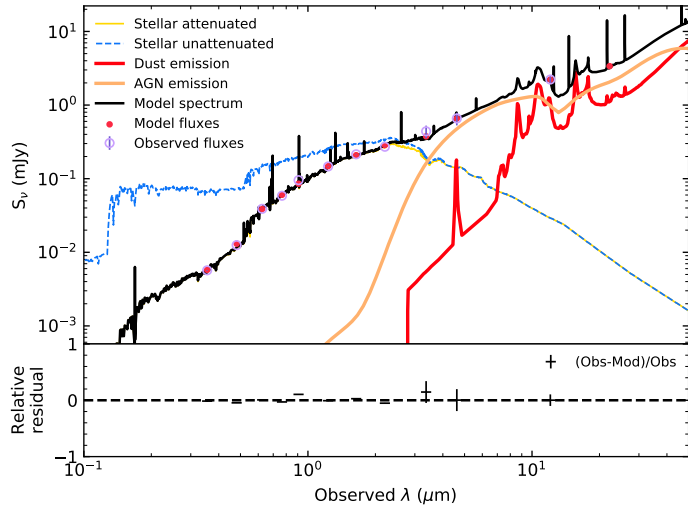
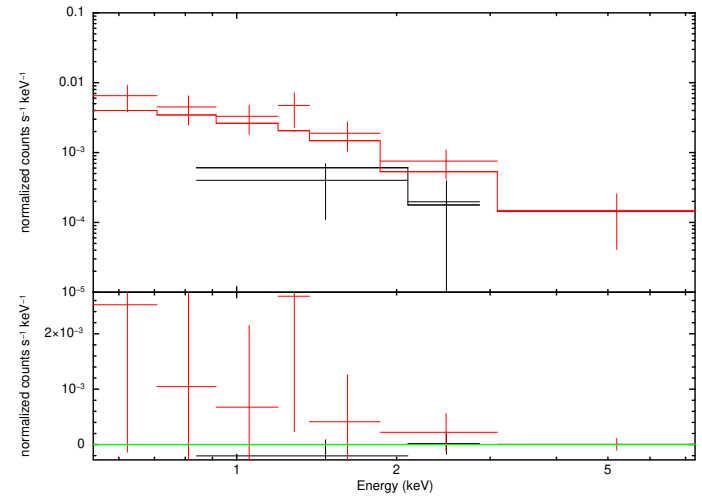
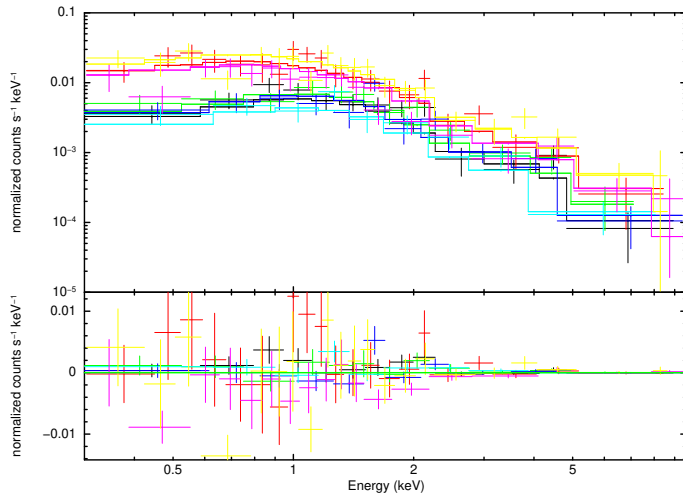


Fig. A.1: J021835.7-053758 (1,2,1), z=0.387

Fig. A.2: J022848.4-044426 (2,2,1), z=1.046

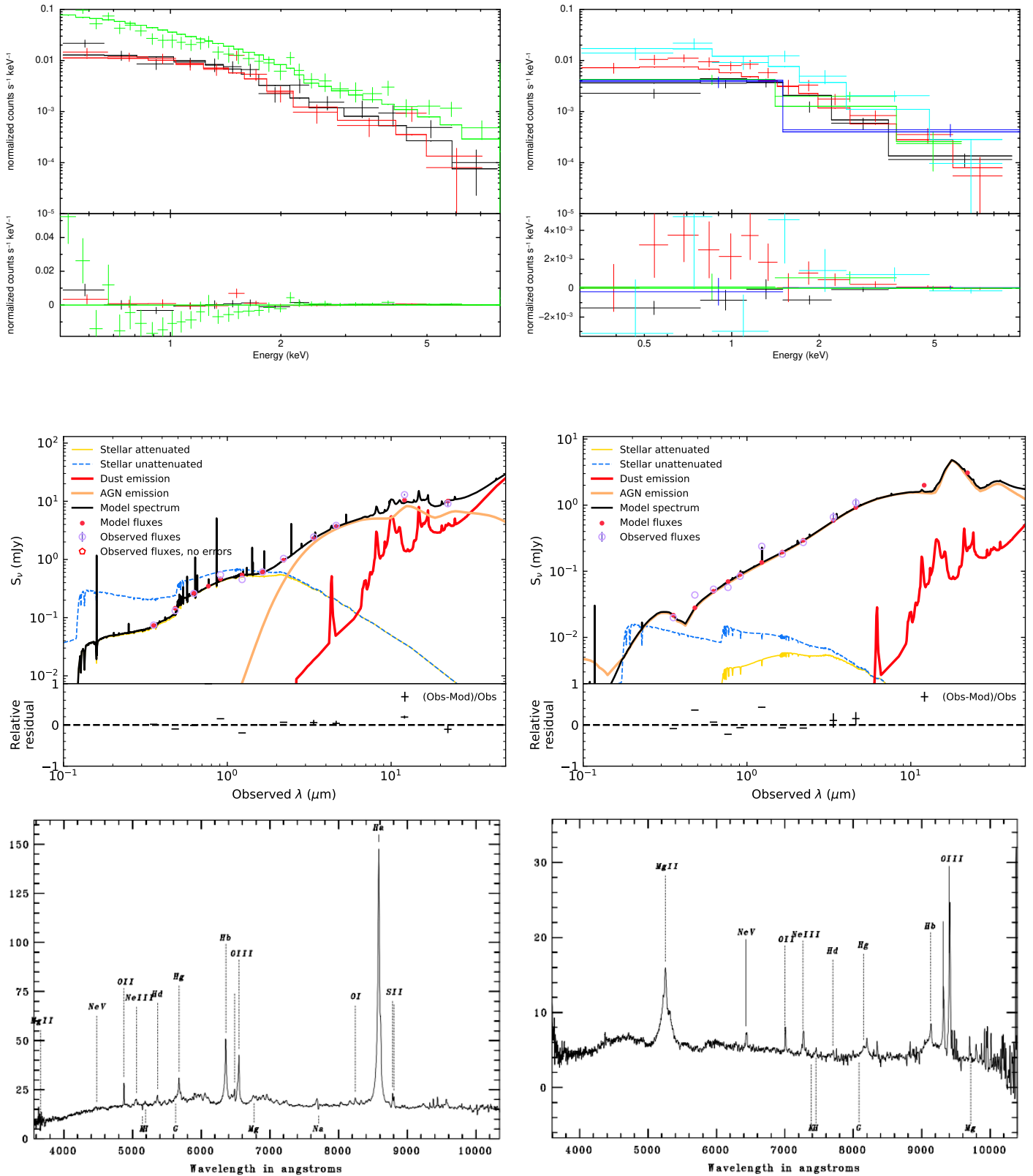

 Fig. A.3: J022928.4-051124 (2,2,1), $z=0.307$

 Fig. A.4: J022809.0-041235 (1,1,1), $z=0.879$

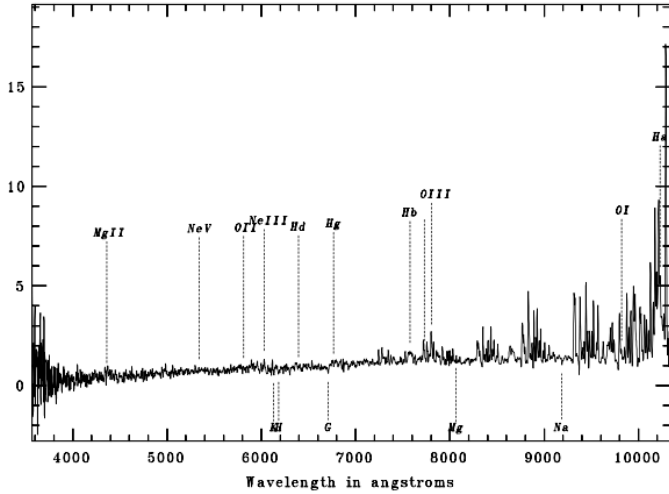
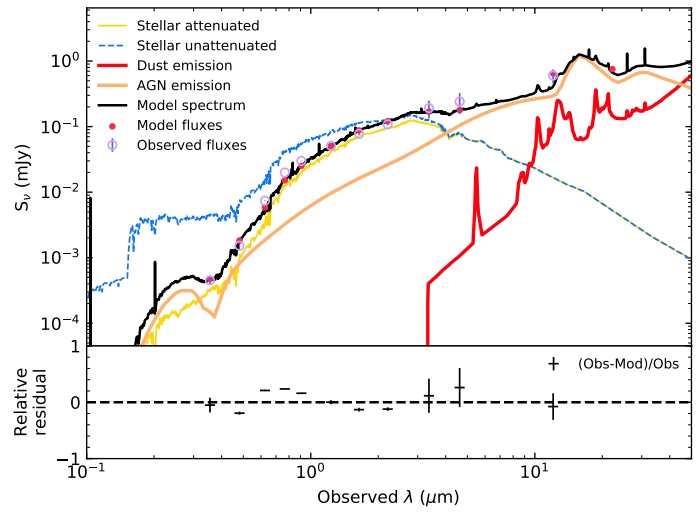
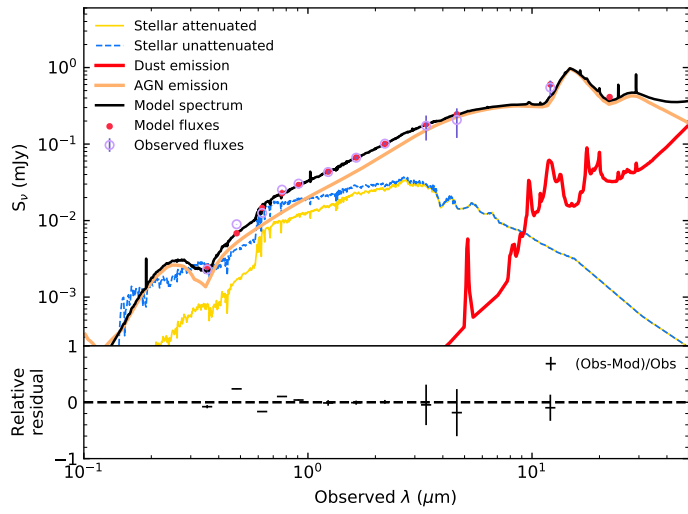
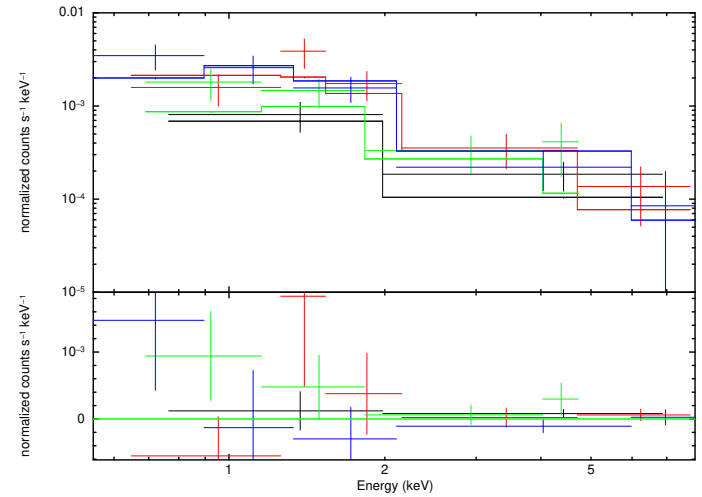
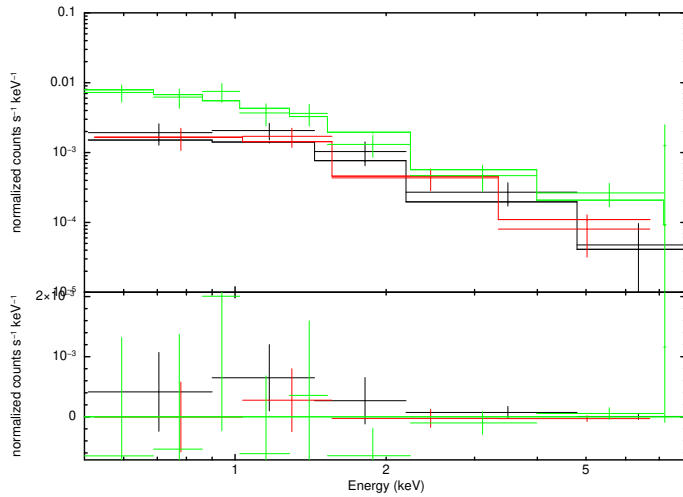


Fig. A.5: J020654.9-064552 (1,2,2), z=1.412

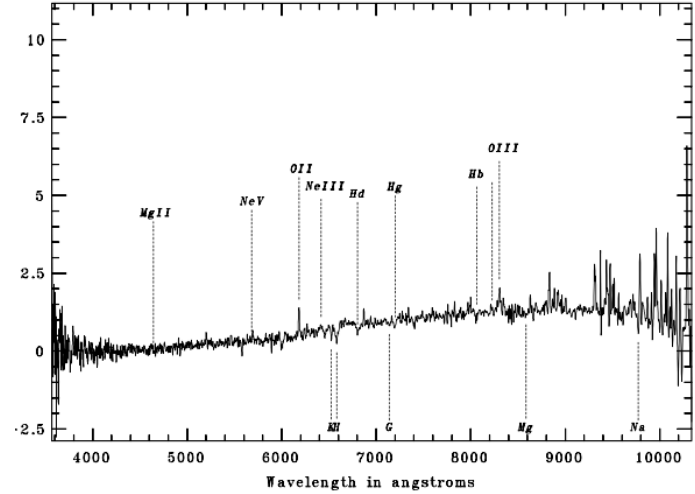
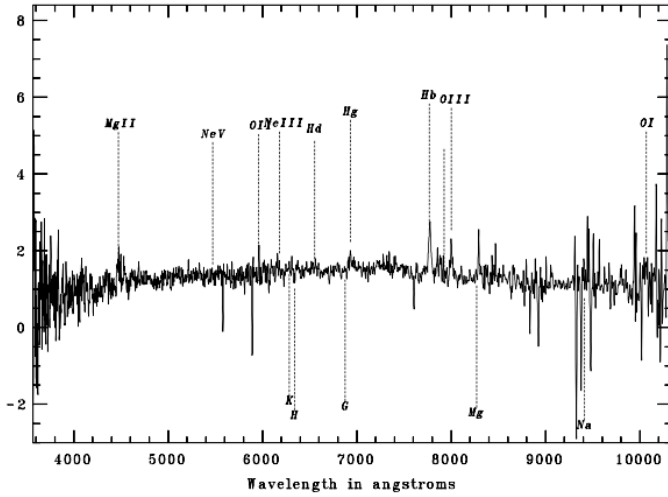
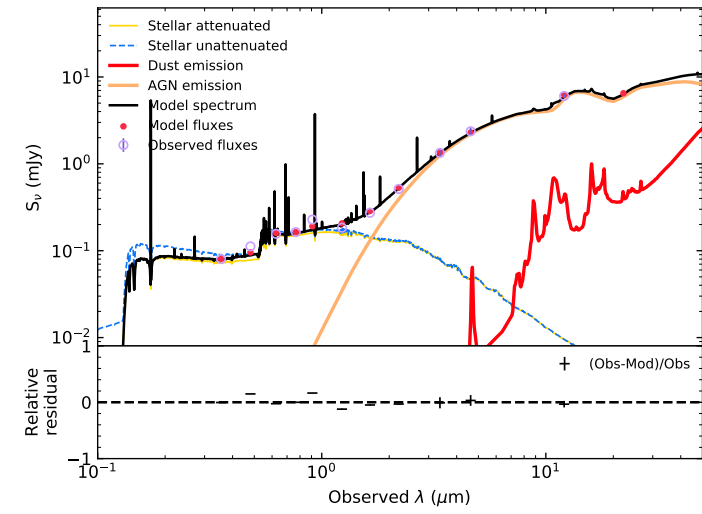
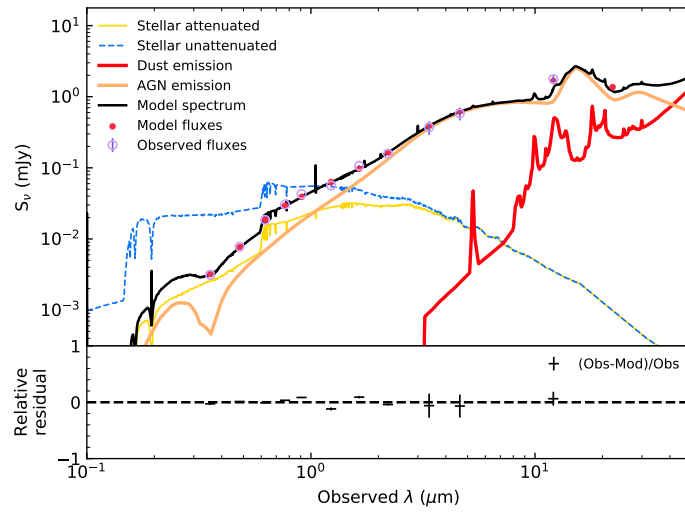
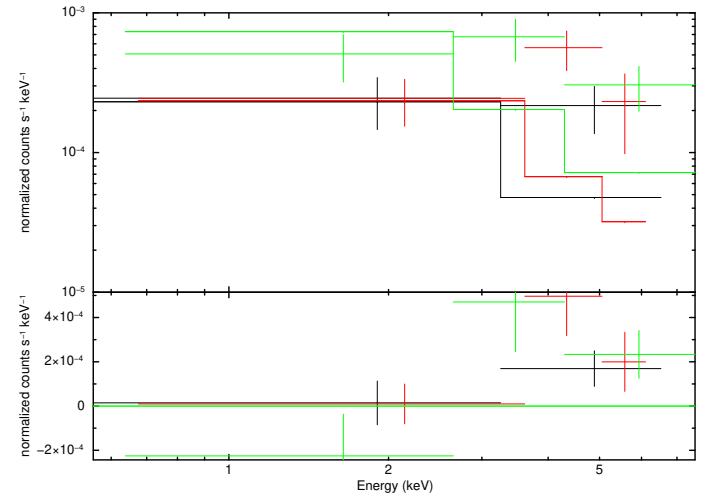
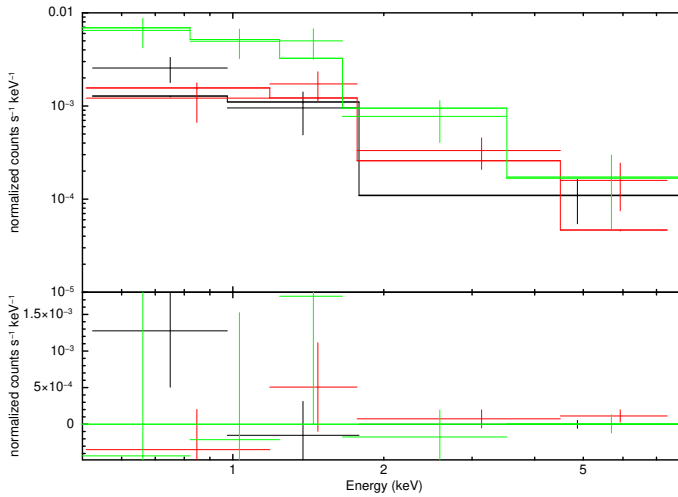
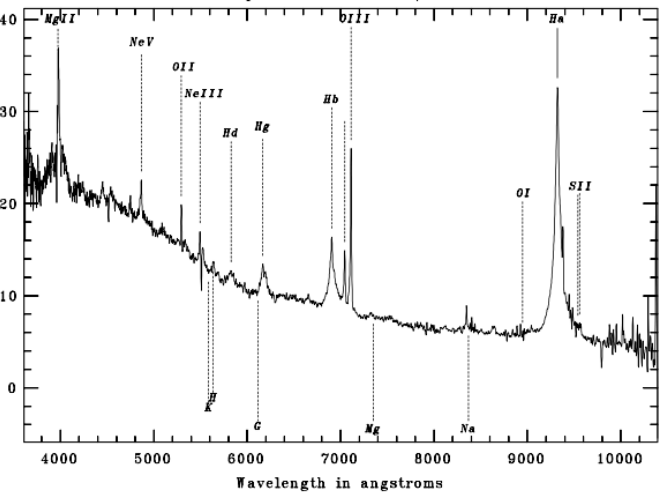


Fig. A.6: J020410.4-063924 (2,2,2), z=0.414


 Fig. A.7: J023315.5-054747 (1,2,2), $z=0.598$

 Fig. A.8: J021337.9-042814 (2,2,1), $z=0.419$

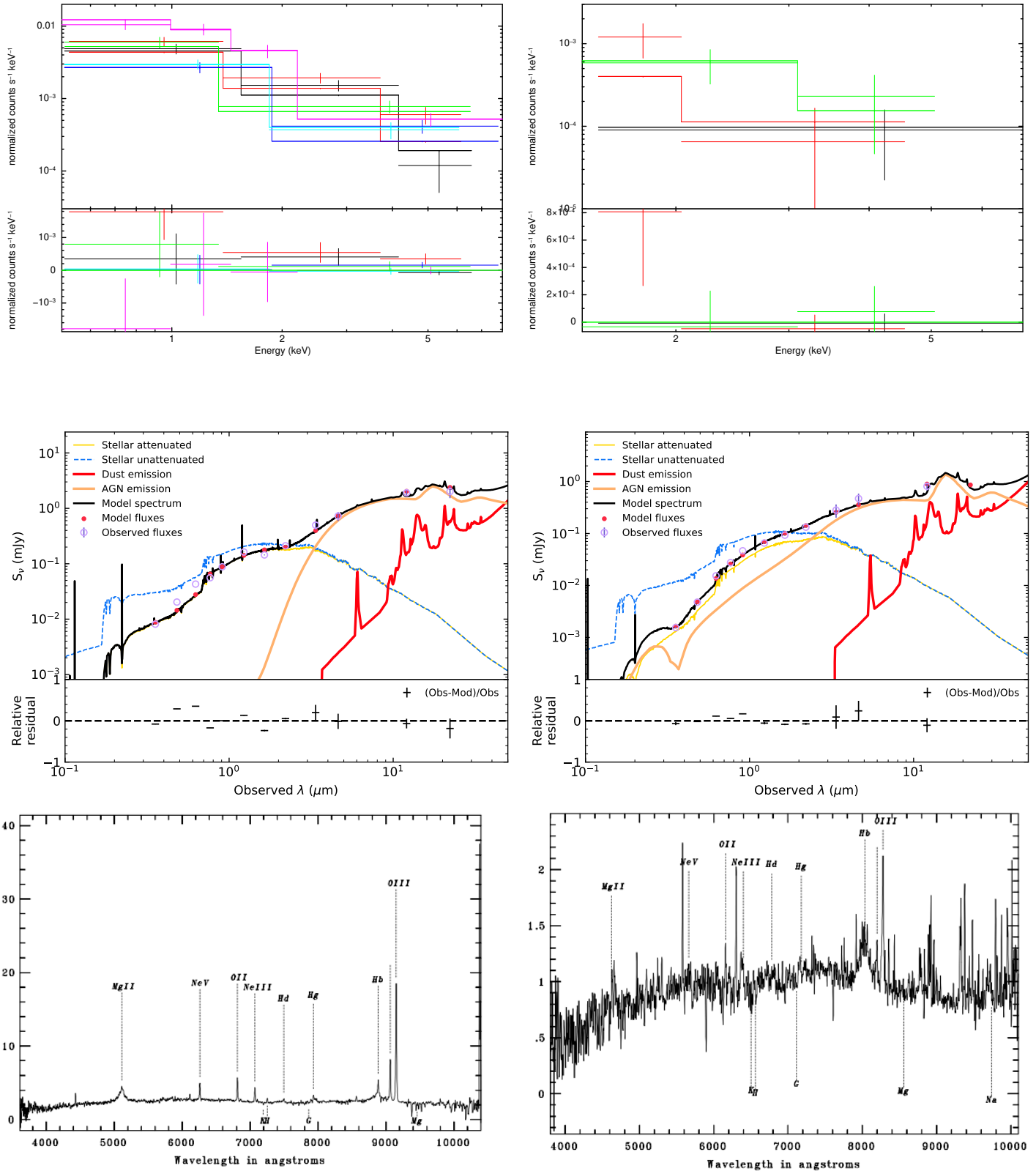


Fig. A.9: J020436.4-042833 (1,2,1), z=0.827

Fig. A.10: J020543.0-051656 (2,2,1), z=0.653

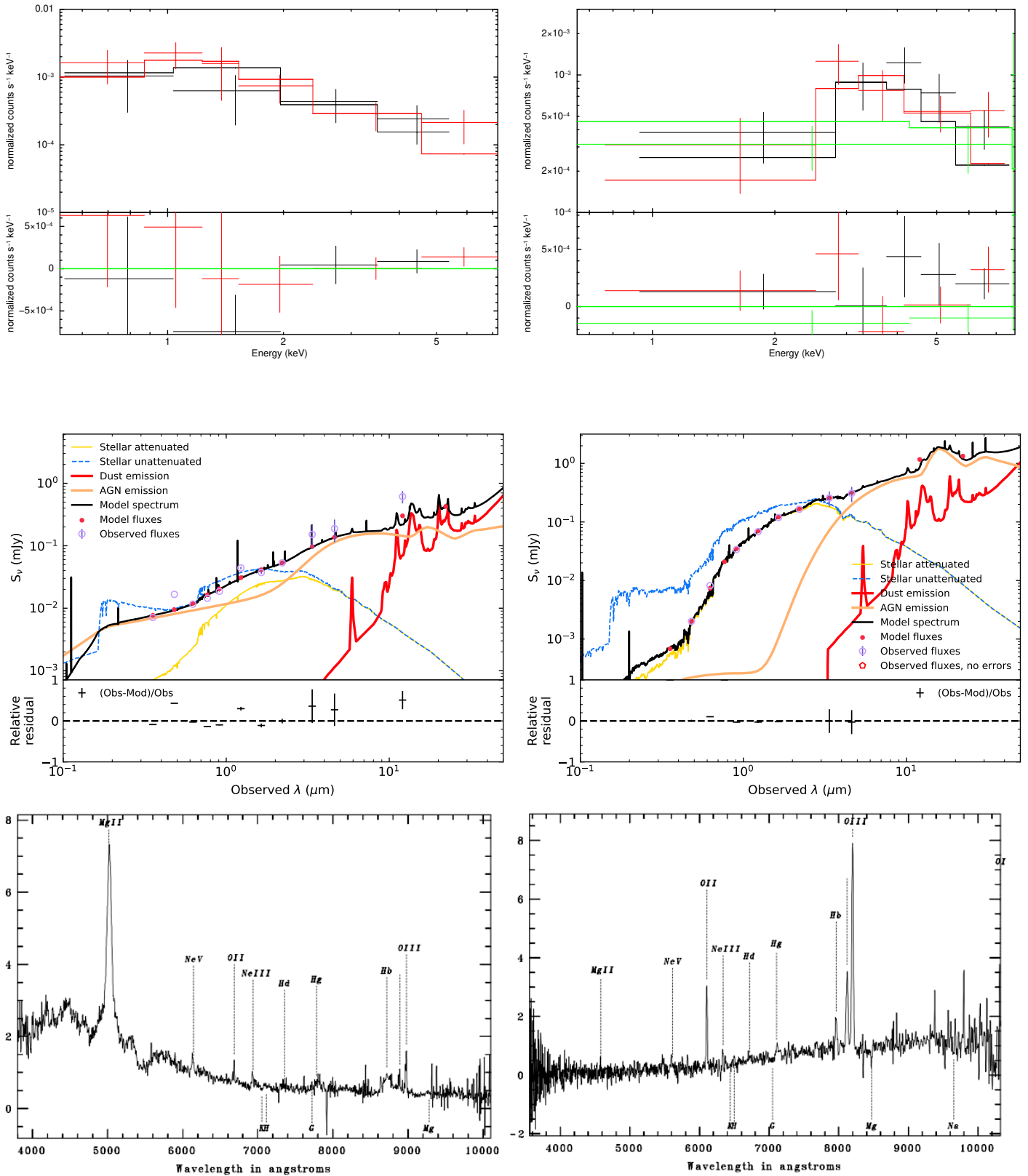
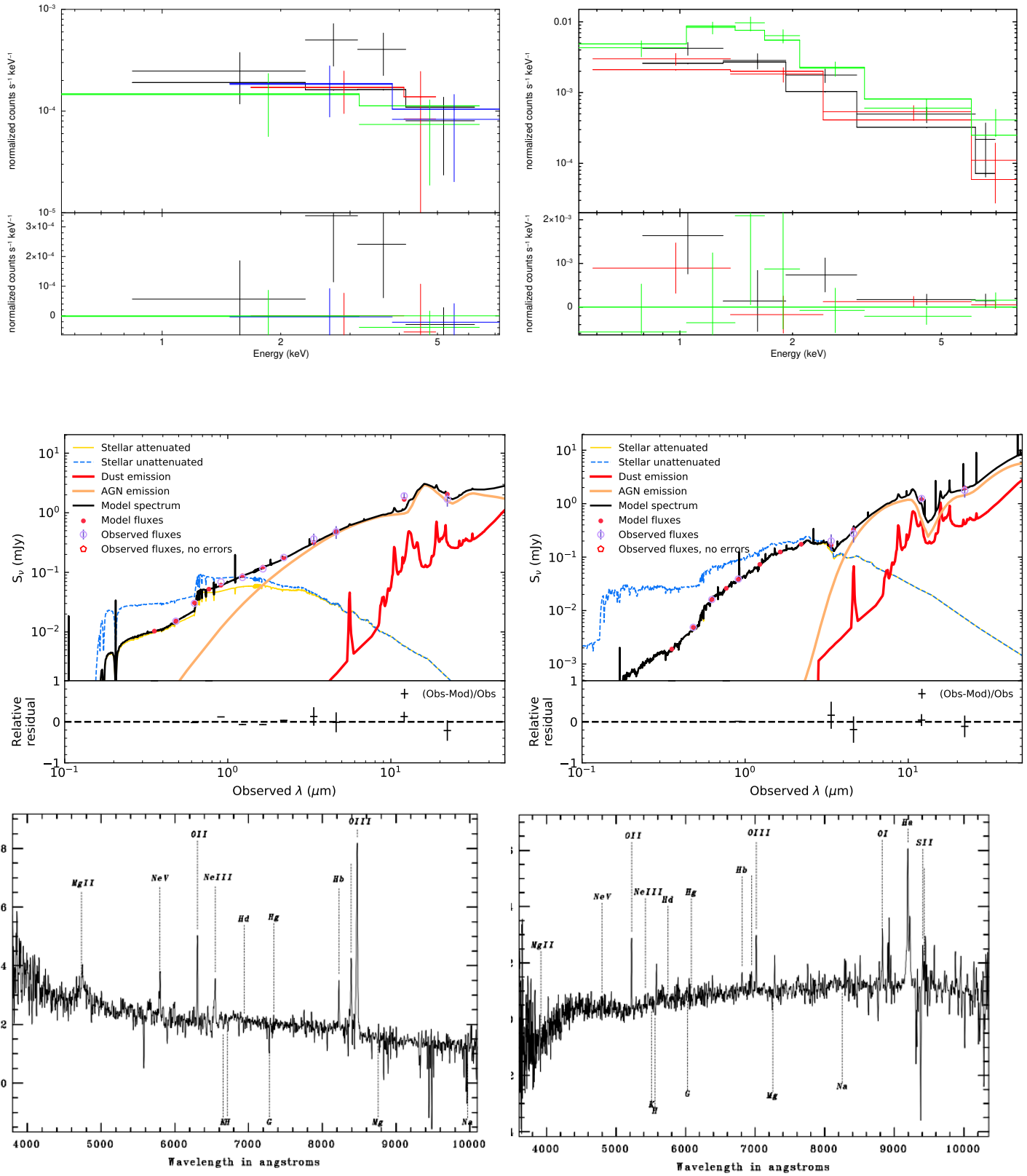


Fig. A.11: J020517.3-051024 (2,0,1), z=0.792

Fig. A.12: J022244.3-030525 (2,2,2), z=0.637

Fig. A.13: J022323.4-031157 (2,2,3), $z=0.691$ Fig. A.14: J022209.6-025023 (2,2,2), $z=0.400$

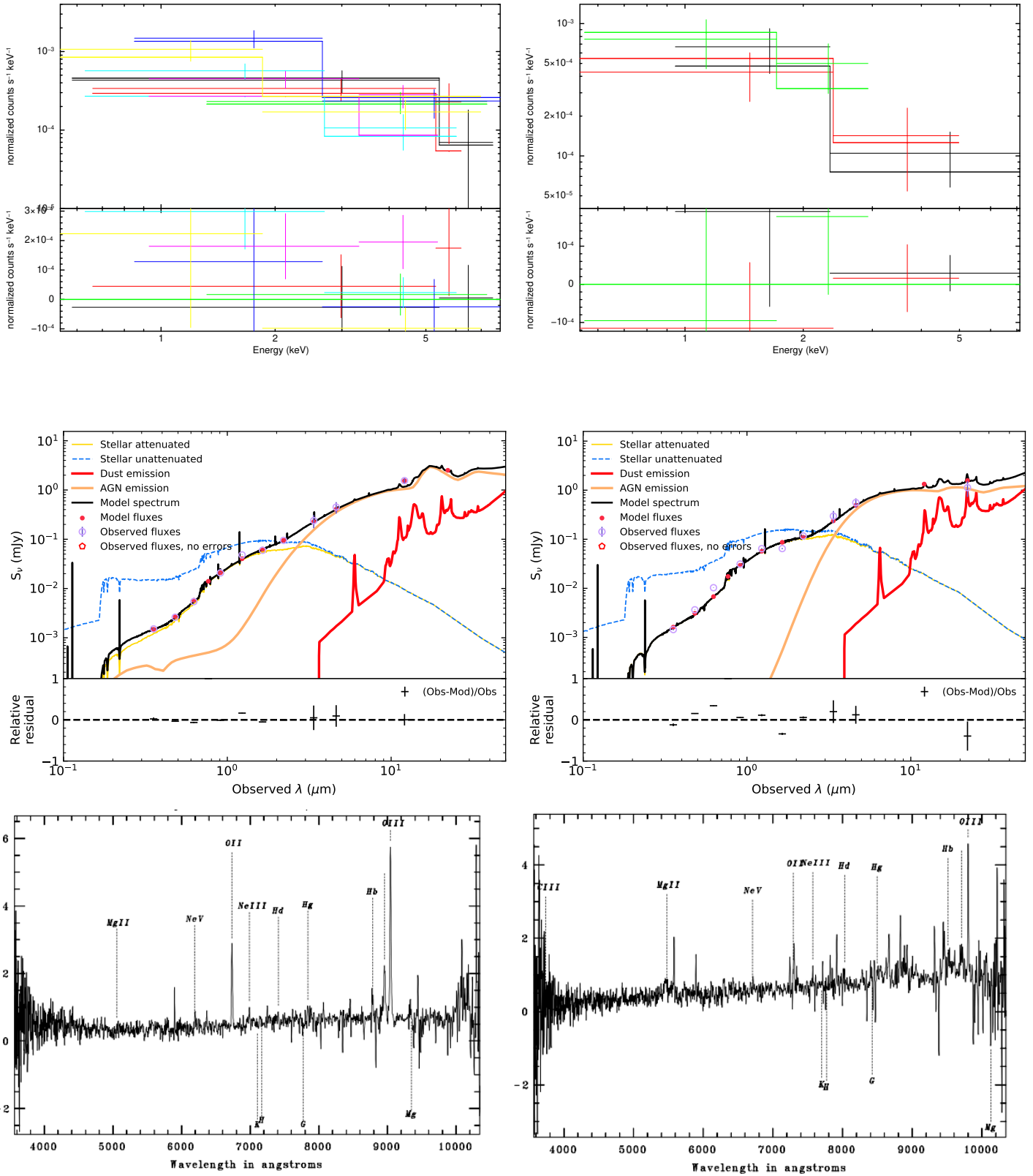
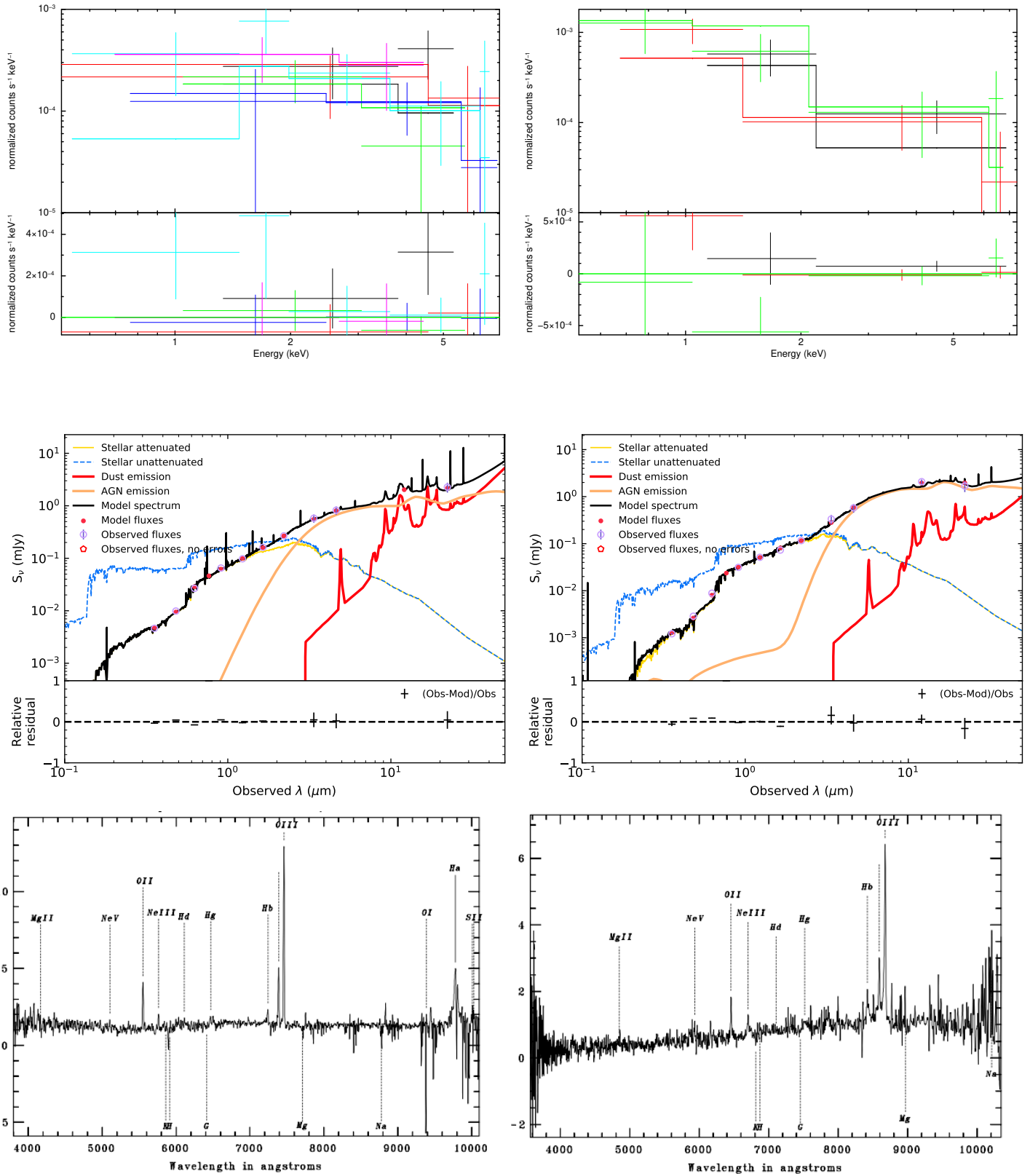


Fig. A.15: J022750.7-052232 (2,2,3), z=0.804

Fig. A.16: J022758.4-053306 (1,2,2), z=0.956

Fig. A.17: J022453.2-054050 (2,2,3), $z=0.488$ Fig. A.18: J022258.8-055757 (1,2,3), $z=0.732$

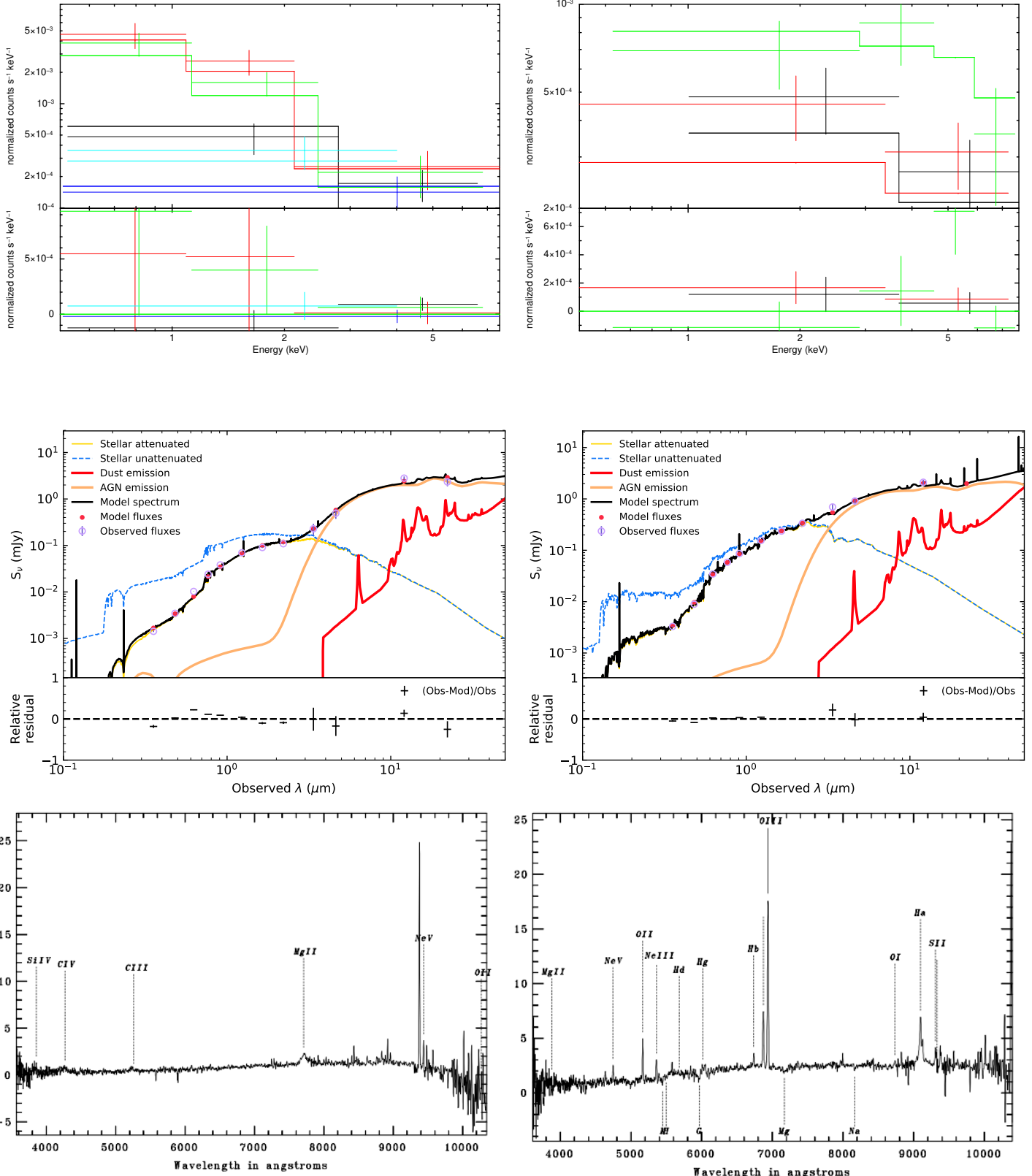
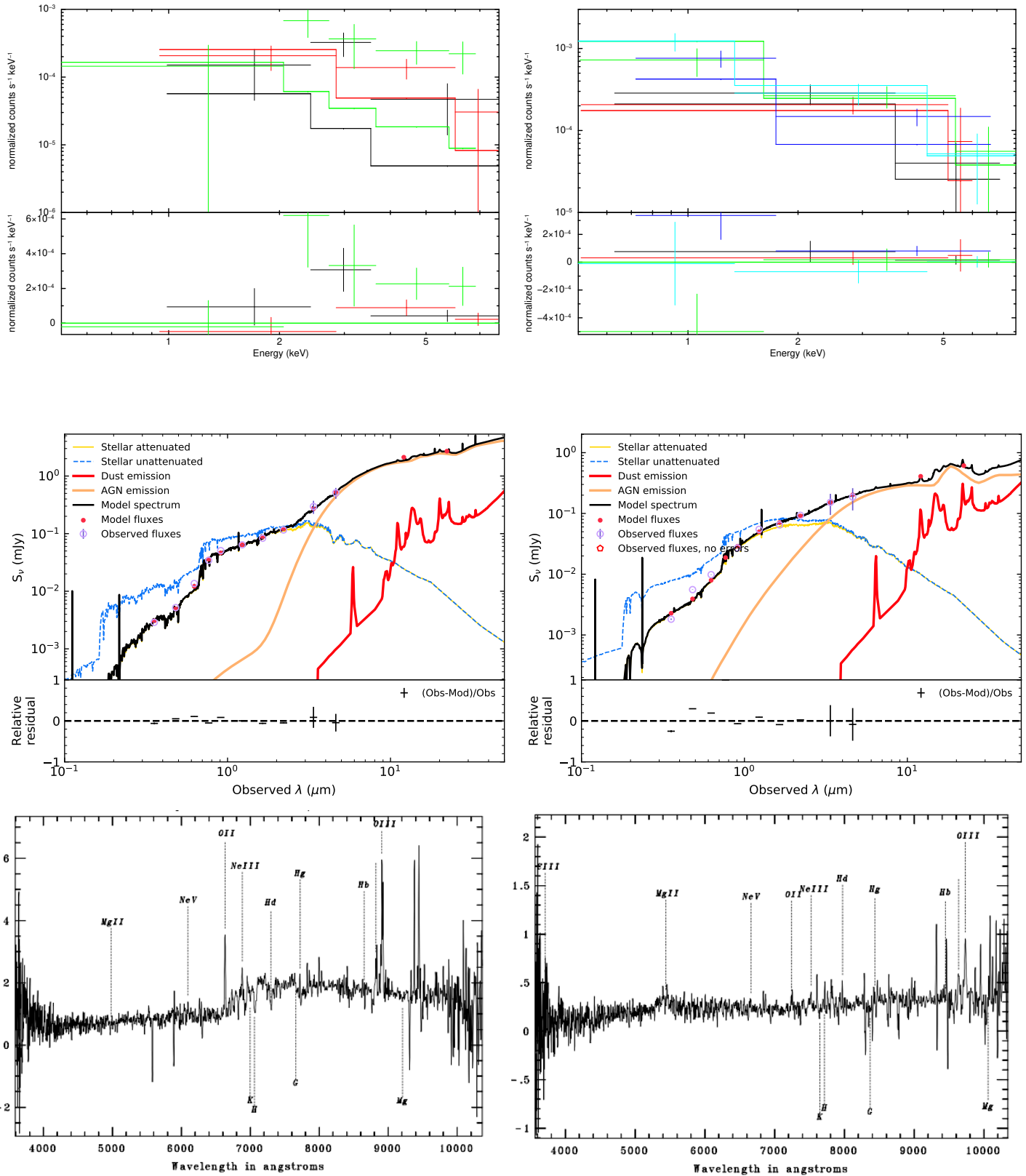

 Fig. A.19: J021844.6-054054 (1,2,3), $z=0.671$

 Fig. A.20: J021523.2-044337 (1,2,2), $z=0.860$

Fig. A.21: J022321.9-045739 (2,2,2), $z=0.779$ Fig. A.22: J022443.6-050905 (2,2,3), $z=0.943$

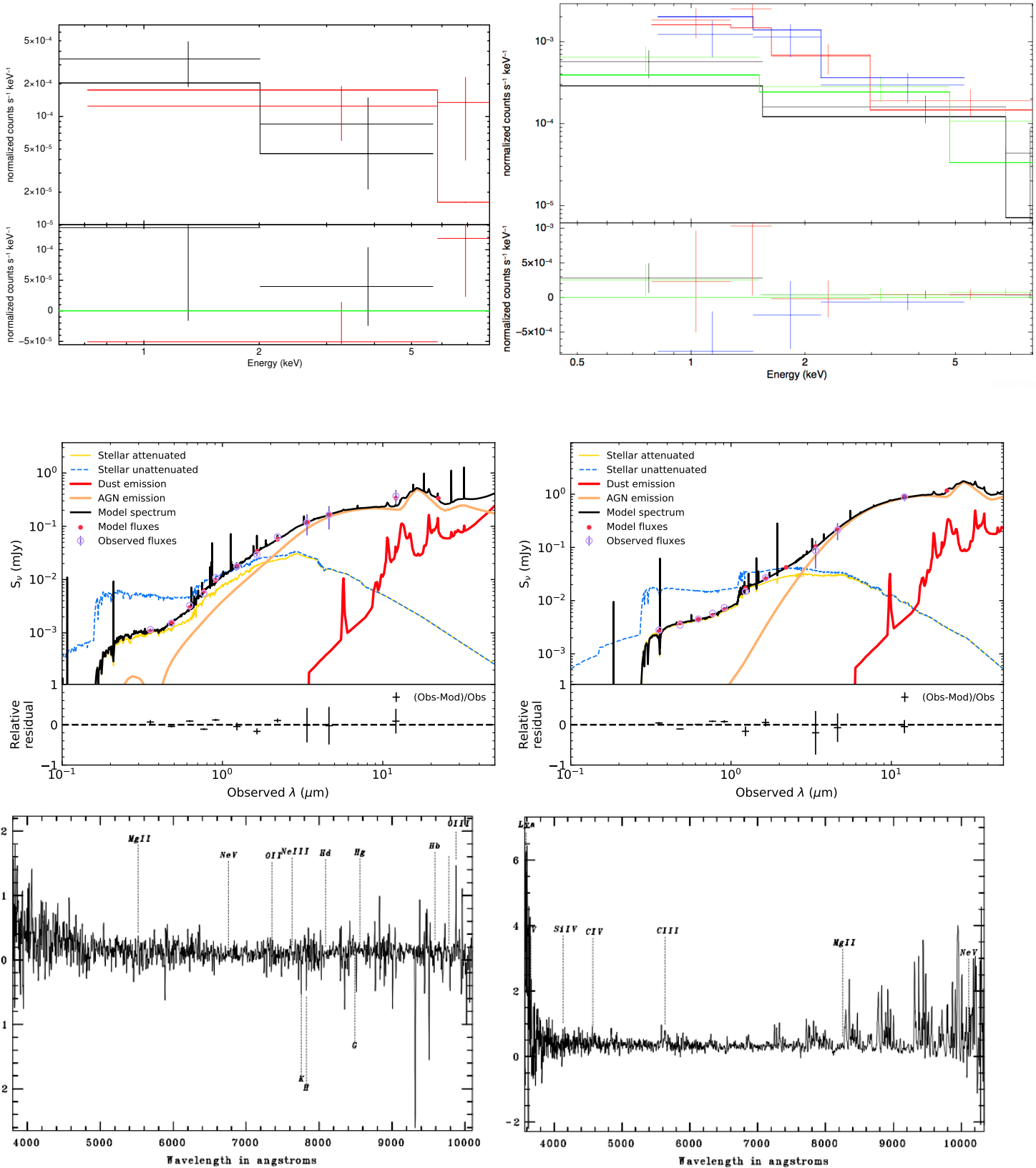

 Fig. A.23: J023418.0-041833 (1,2,0), $z=0.582$

 Fig. A.24: J020543.7-063807 (1,2,0), $z=0.772$

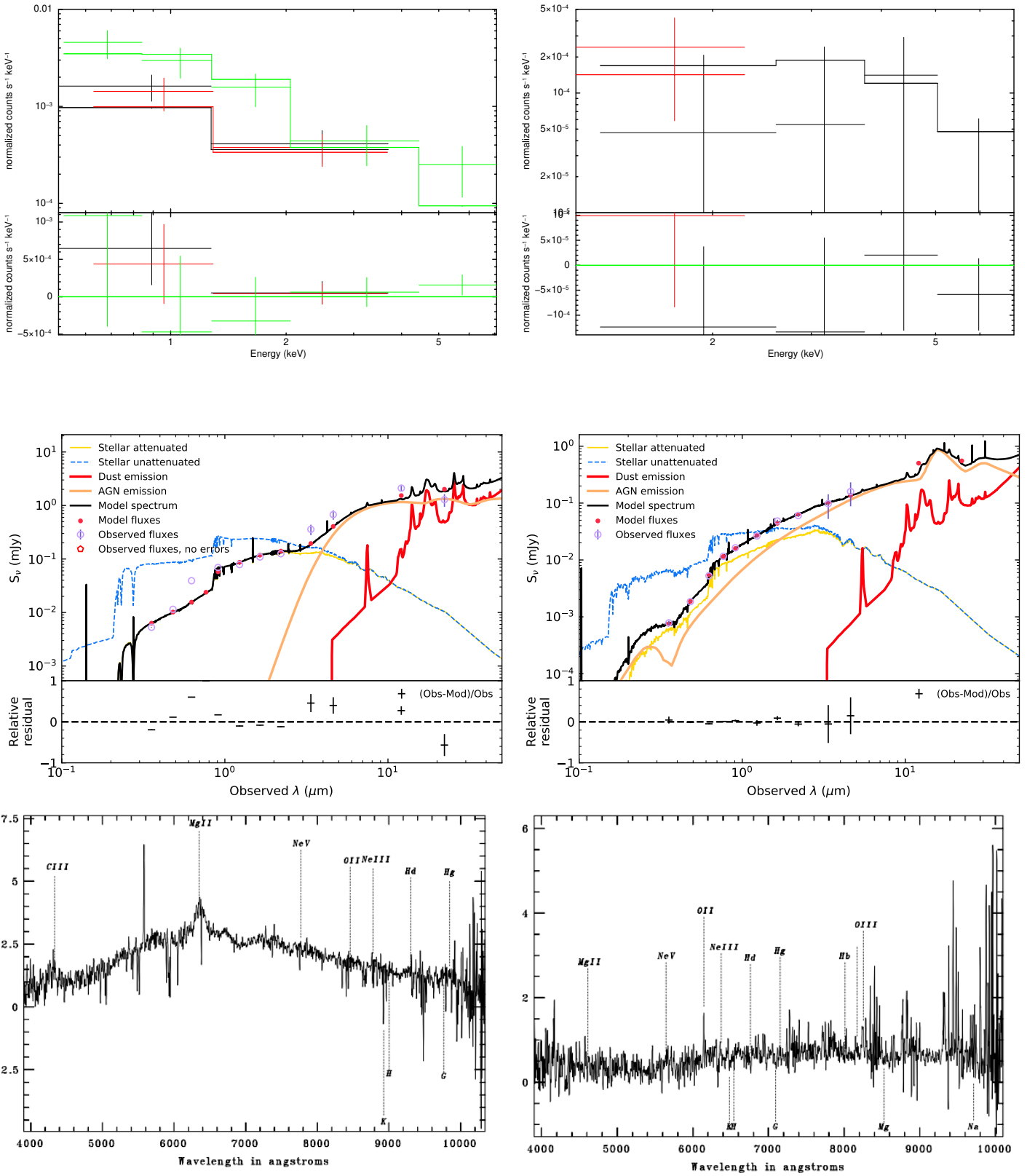
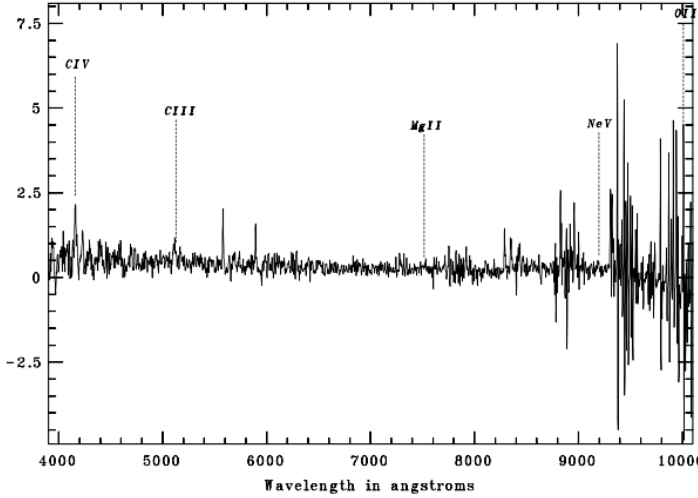
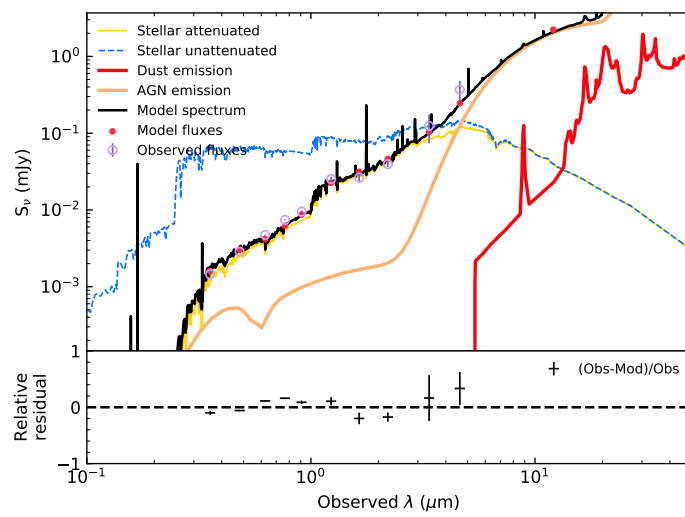
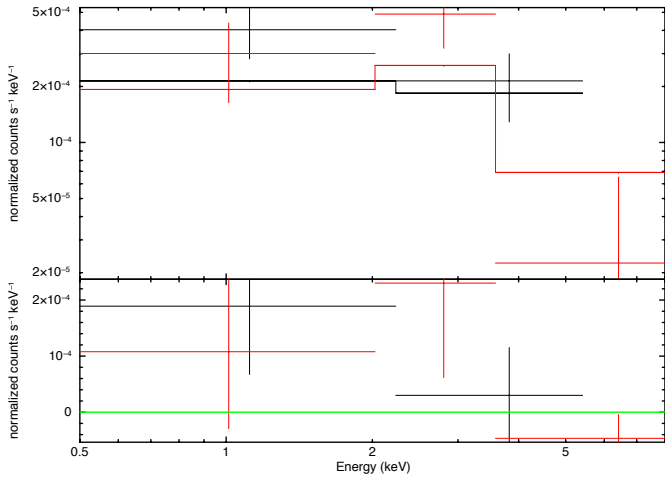
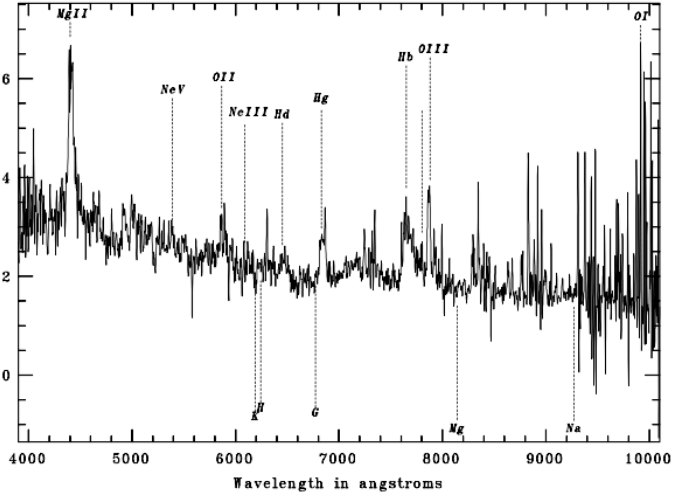
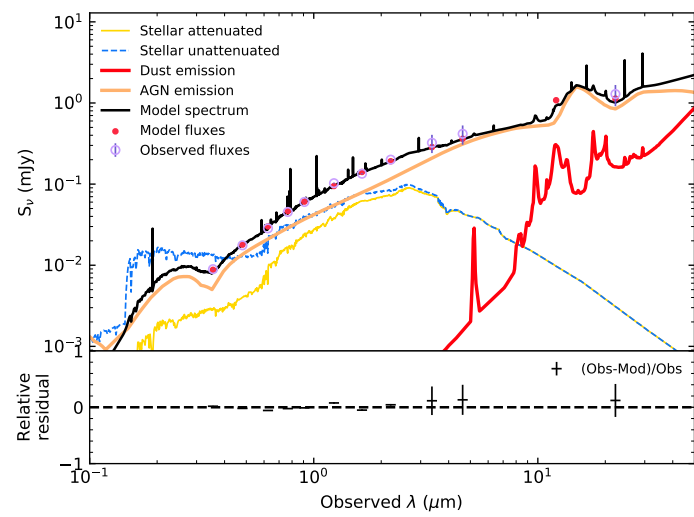
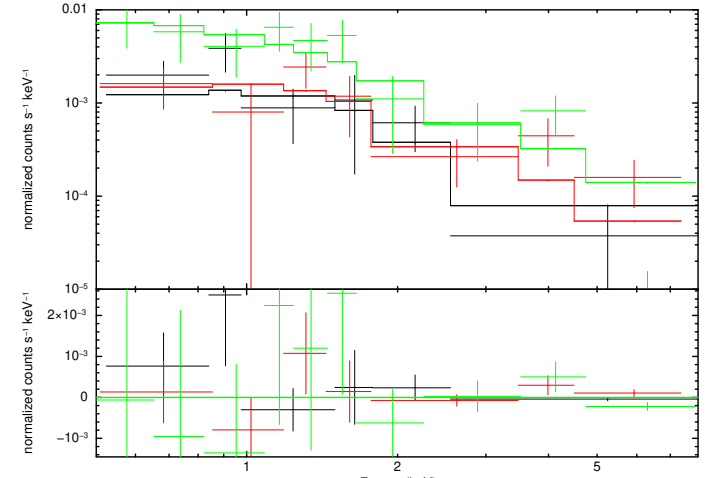
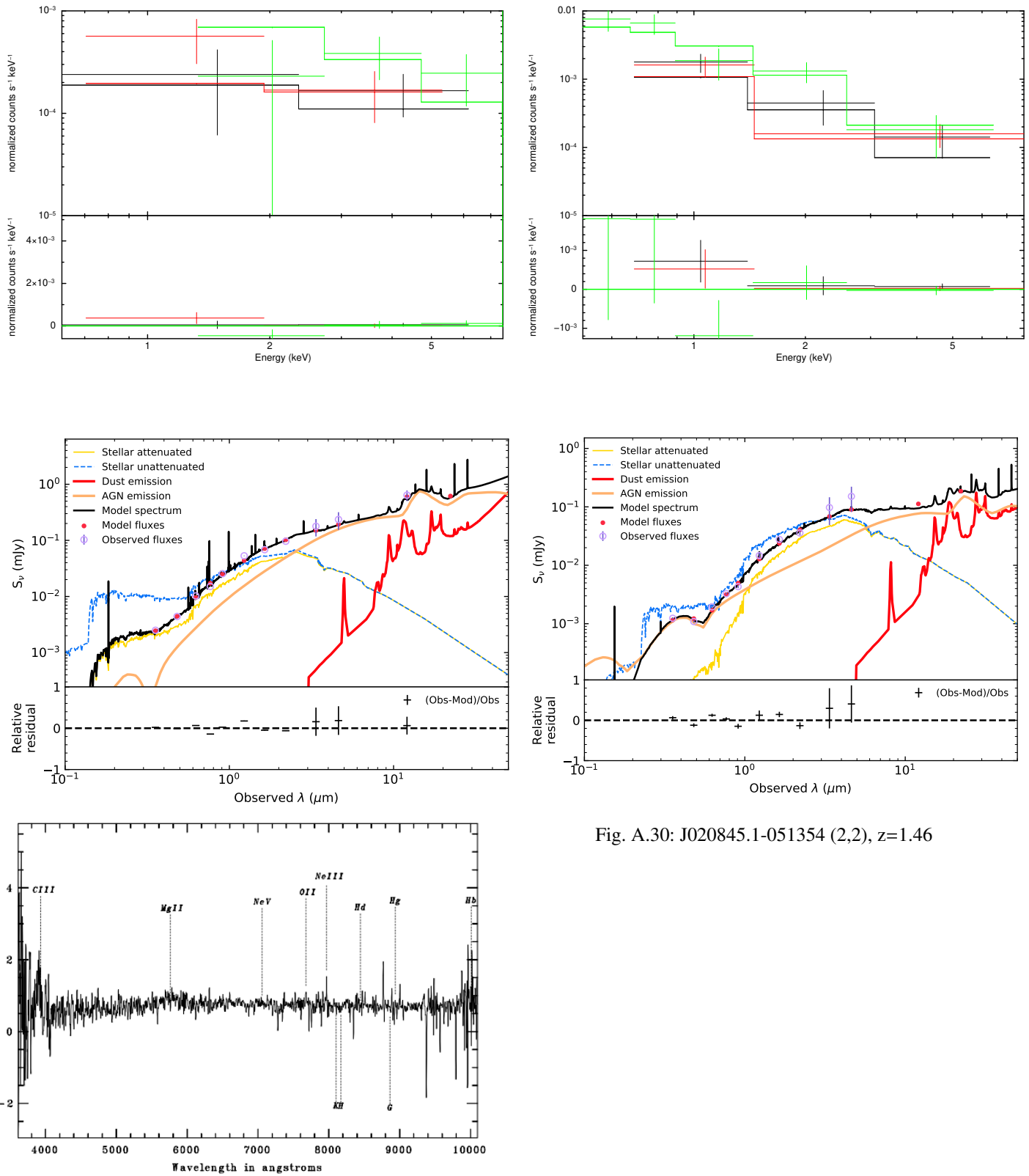


Fig. A.25: J022932.6-055438 (1,2,1), z=1.263

Fig. A.26: J021239.2-054816 (2,2,0), z=0.711


 Fig. A.27: J021511.4-060805 (2,2,1), $z=0.772$

 Fig. A.28: J021808.8-055630 (1,0,1), $z=0.572$

Fig. A.29: J022538.9-040821 (2,2,1), $z=0.733$

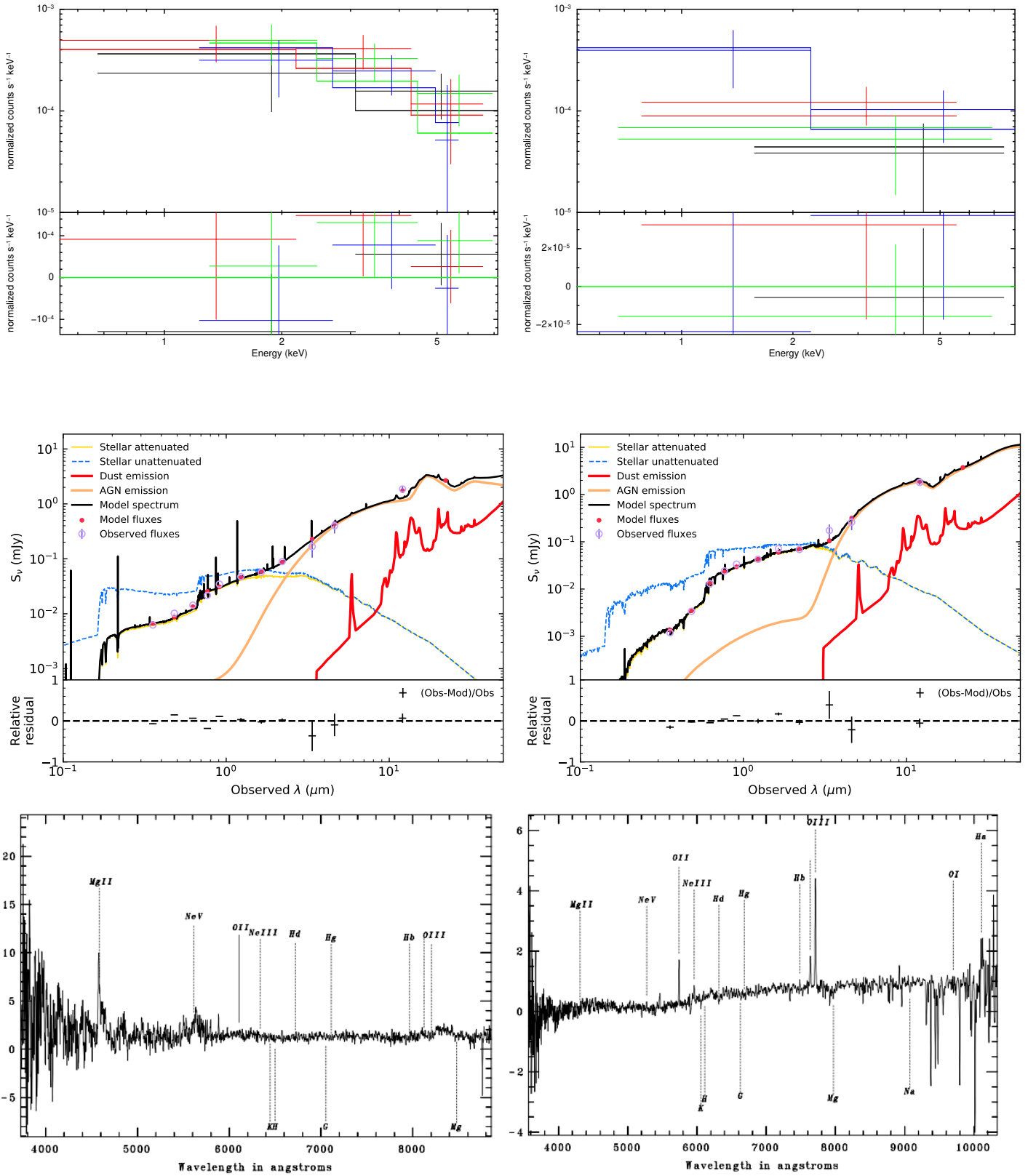

 Fig. A.31: J020953.9-055102 (2,2,1), $z=0.642$

 Fig. A.32: J020806.6-055739 (2,2,2), $z=0.539$

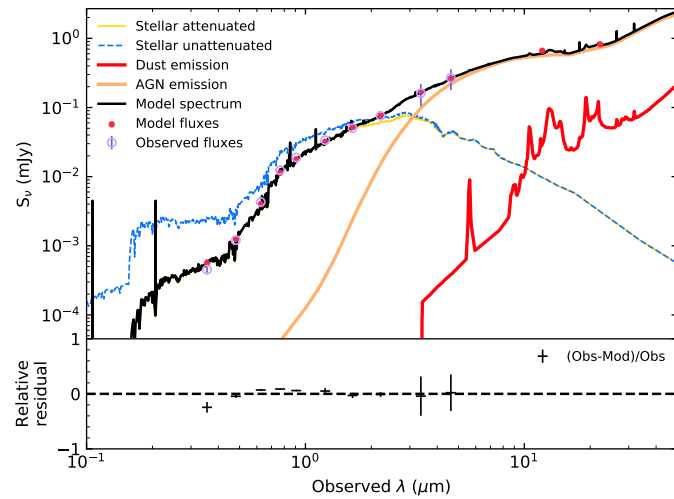
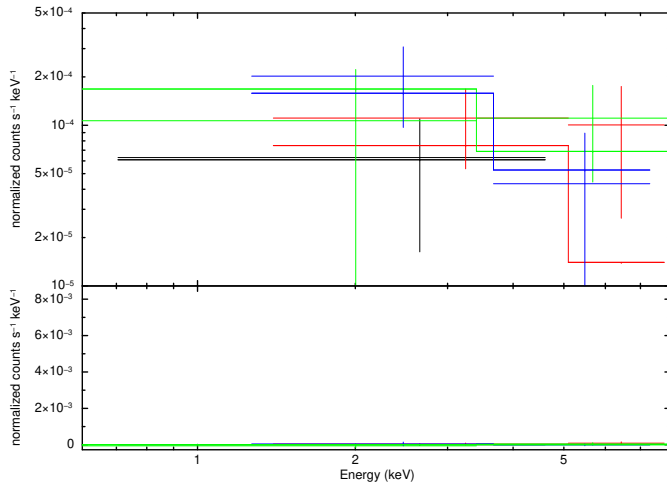


Fig. A.33: J021509.0-054305 (2,2), z=0.70

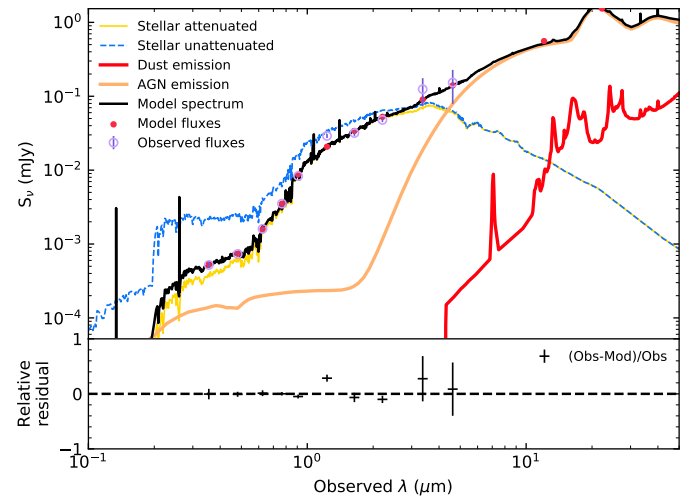
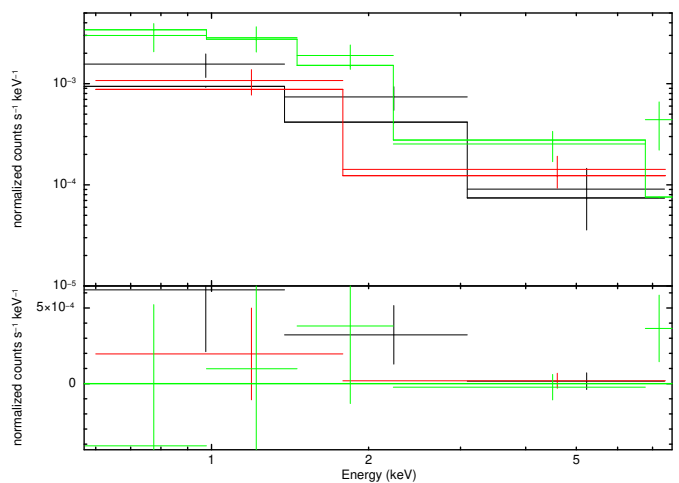
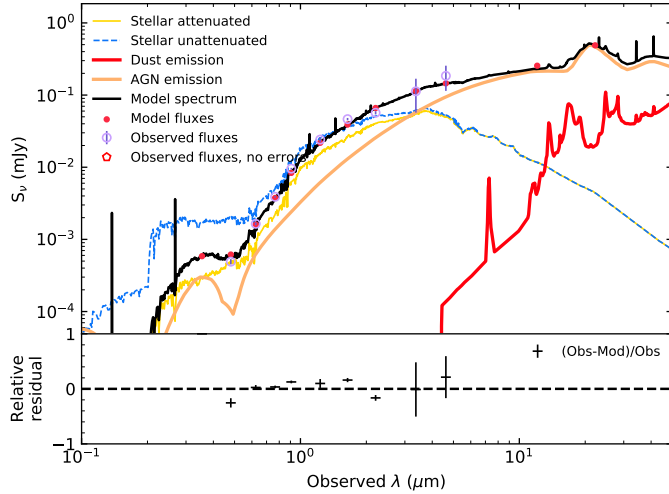
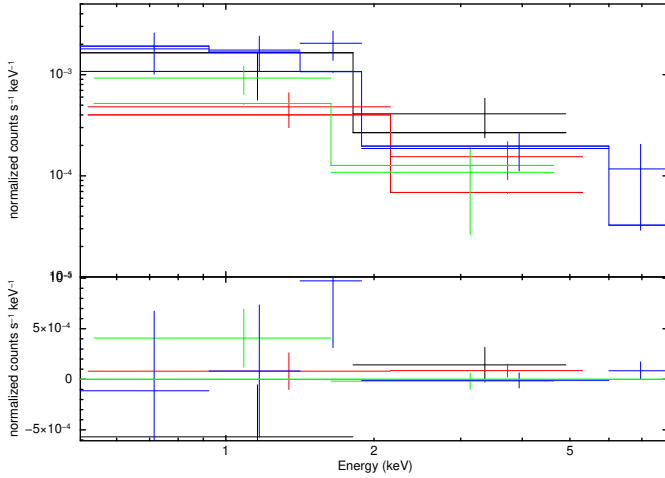
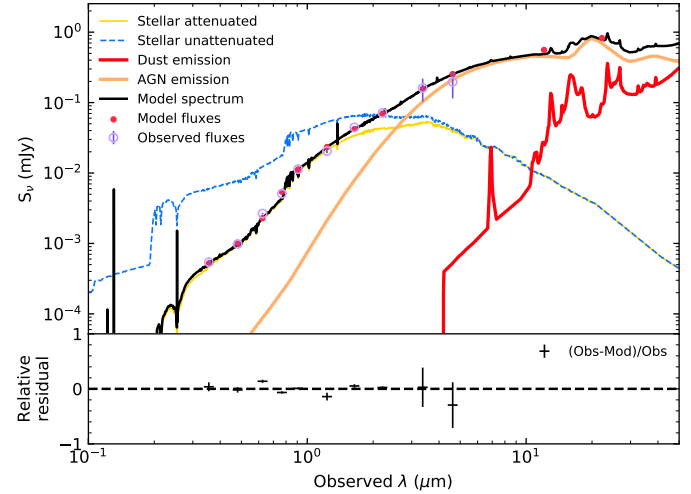
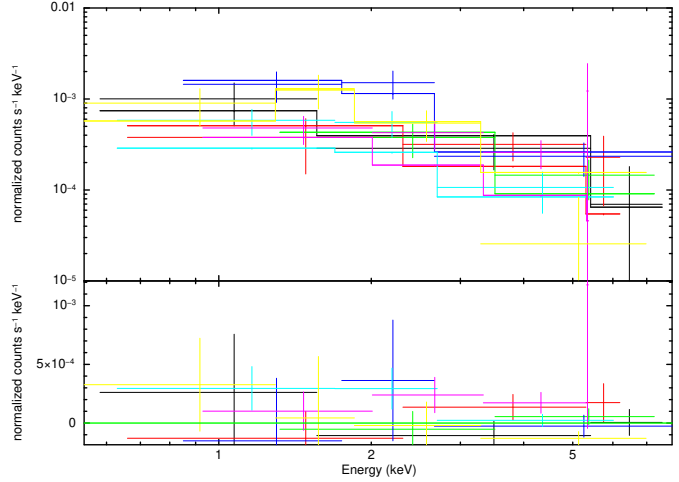


Fig. A.34: J021512.9-060558 (2,2), z=1.14


 Fig. A.35: J020529.5-051100 (2,2), $z=1.20$

 Fig. A.36: J022404.0-035730 (2,2), $z=0.17$

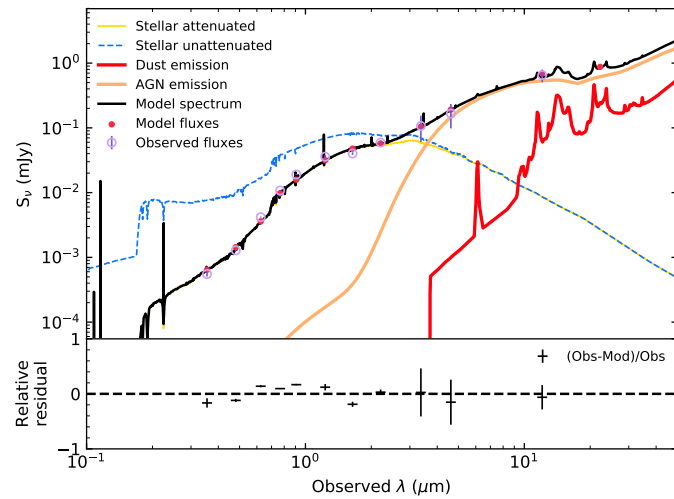
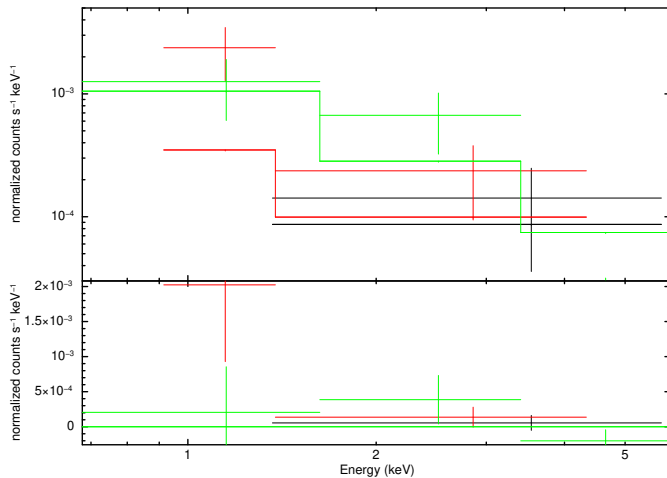


Fig. A.37: J023501.0-055234 (2,2), z=0.85

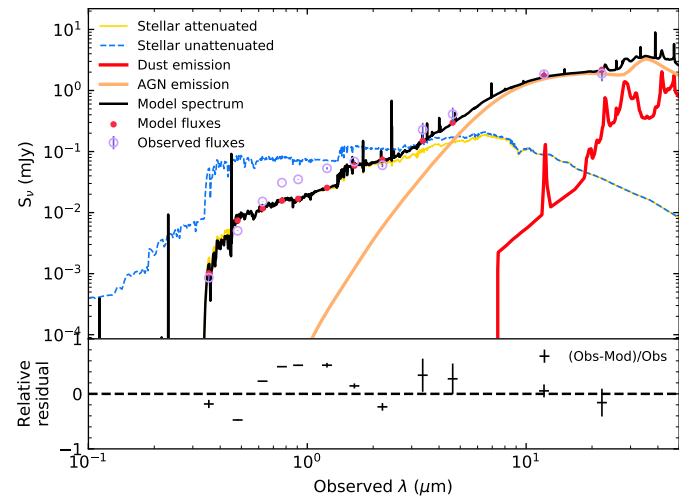
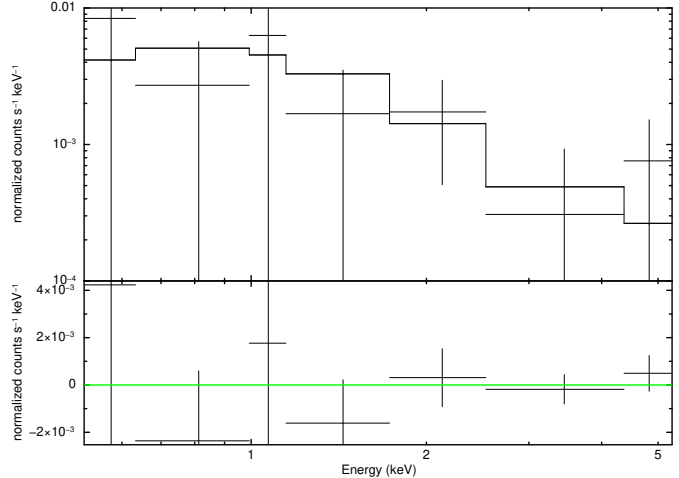
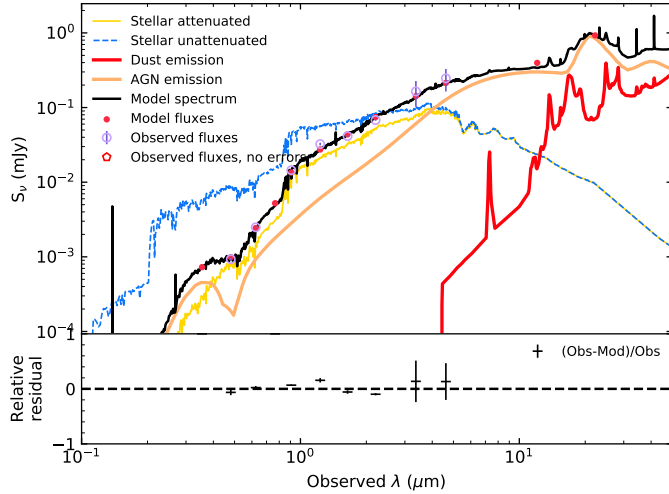
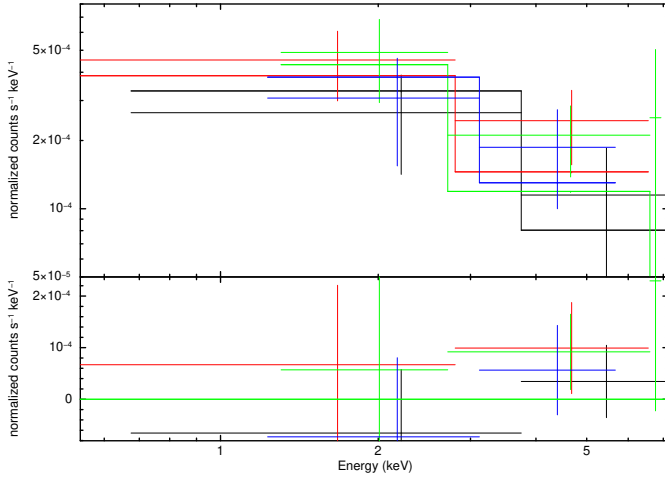
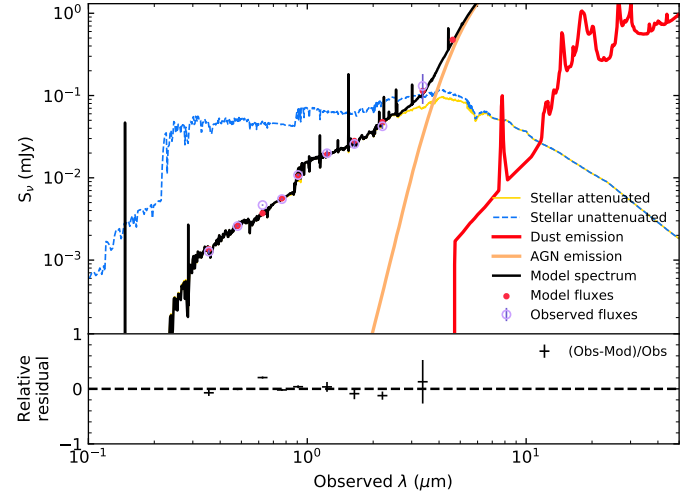
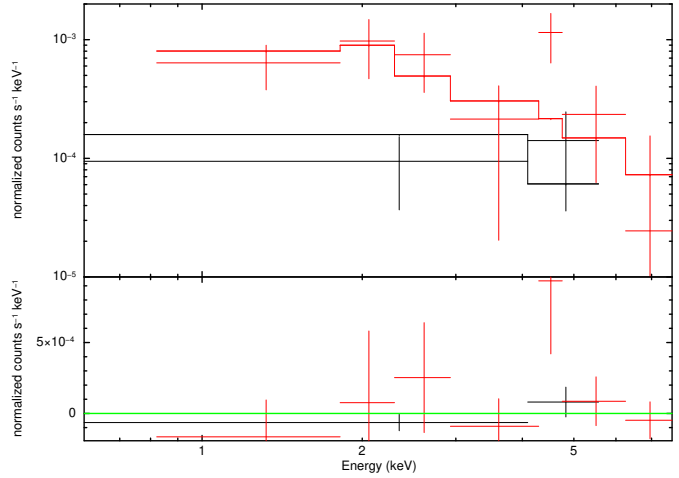


Fig. A.38: J020210.6-041129 (2,2), z=2.71


 Fig. A.39: J022650.3-025752 (2,2), $z=1.21$

 Fig. A.40: J021303.7-040704 (2,2), $z=1.35$

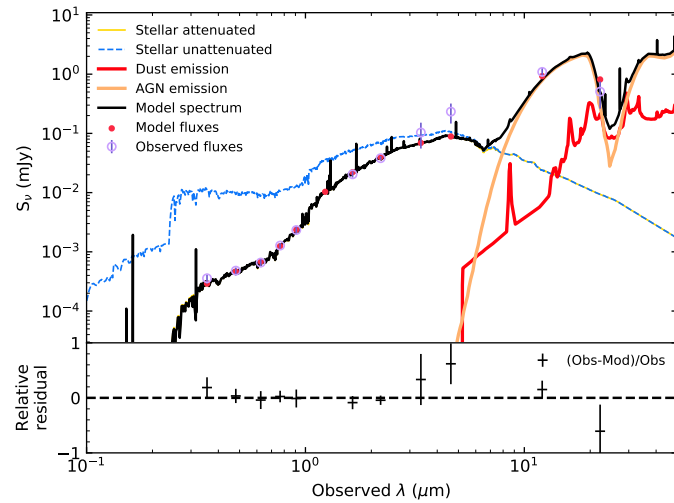
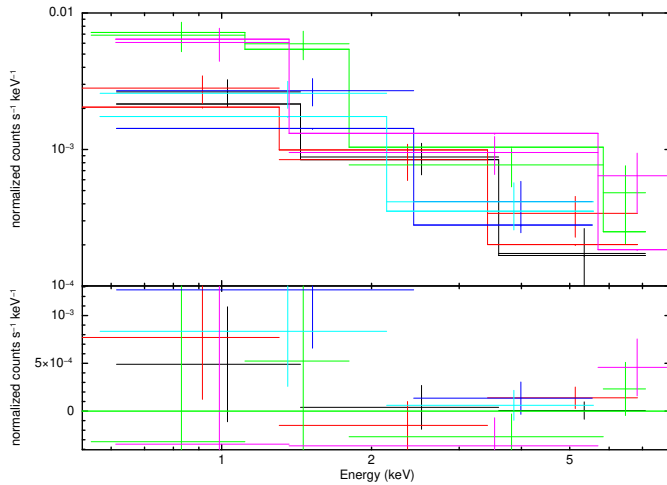


Fig. A.41: J023357.7-054819 (2,2), z=1.60

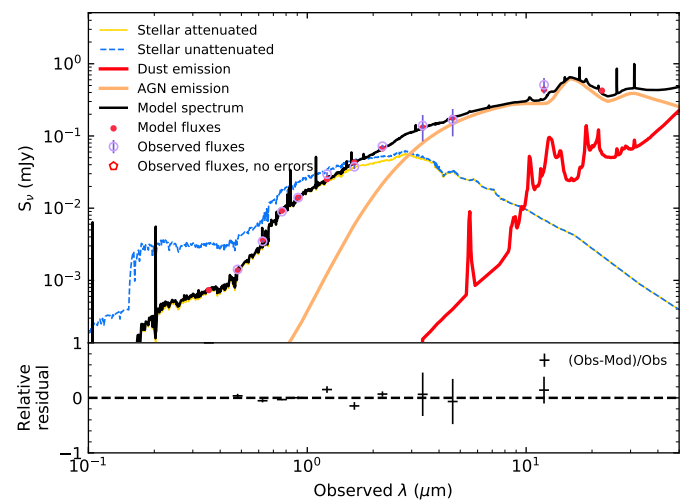
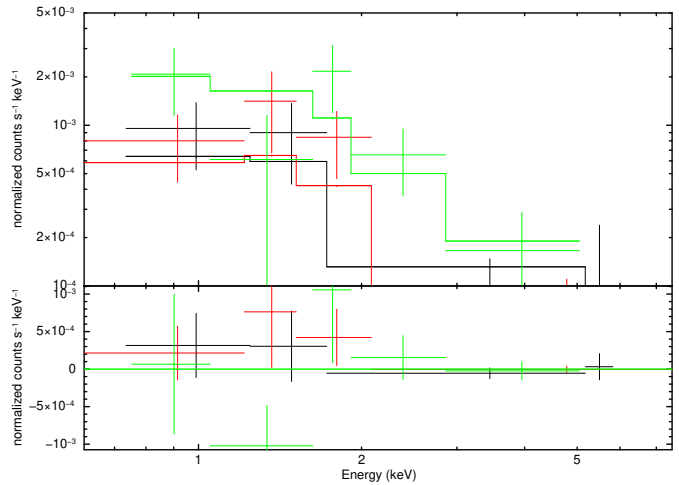
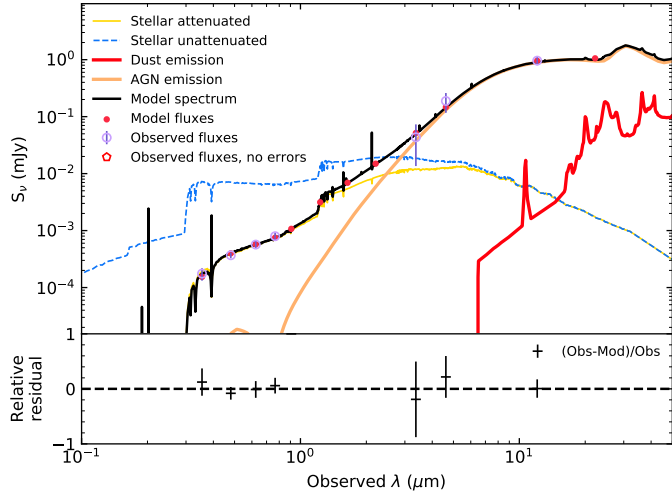
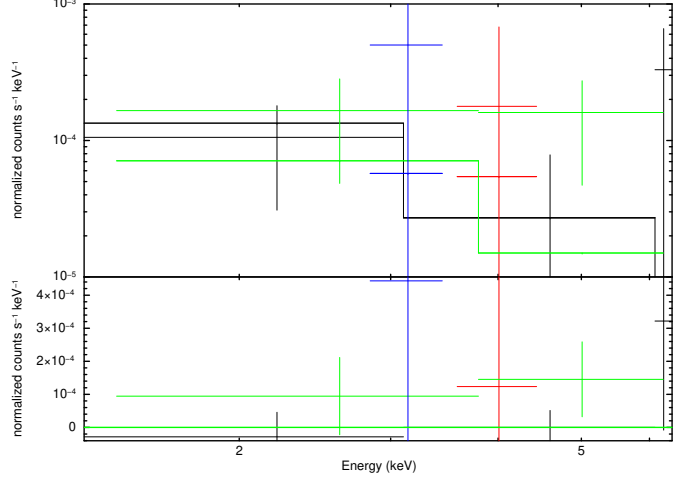
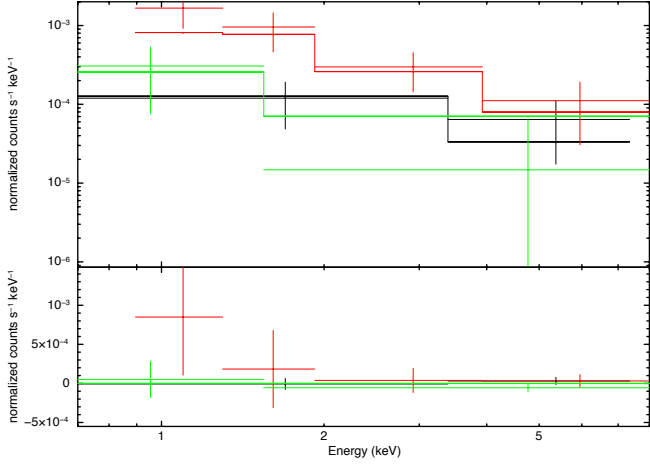
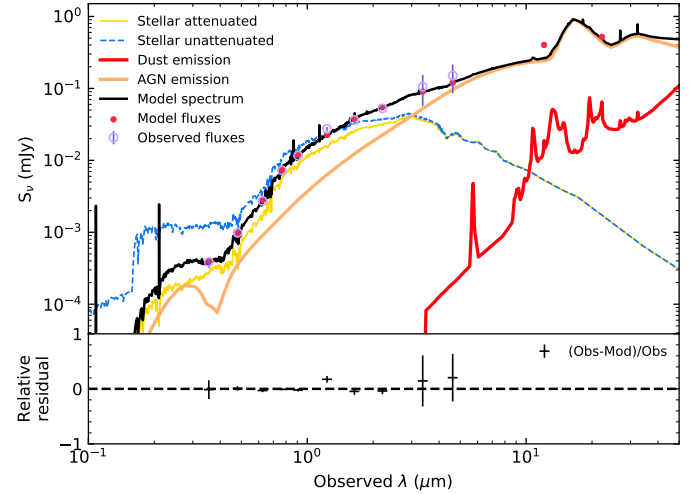


Fig. A.42: J020335.0-064450 (2,2), z=0.67


 Fig. A.43: J020823.4-040652 (1,2), $z=2.23$

 Fig. A.44: J020135.4-050847 (1,2), $z=0.73$

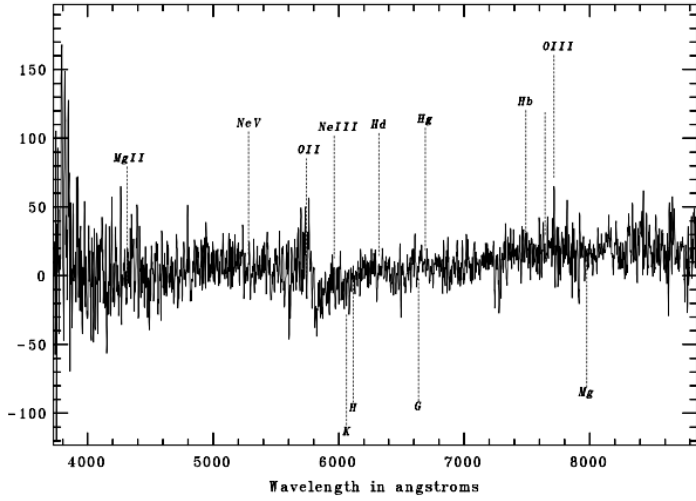
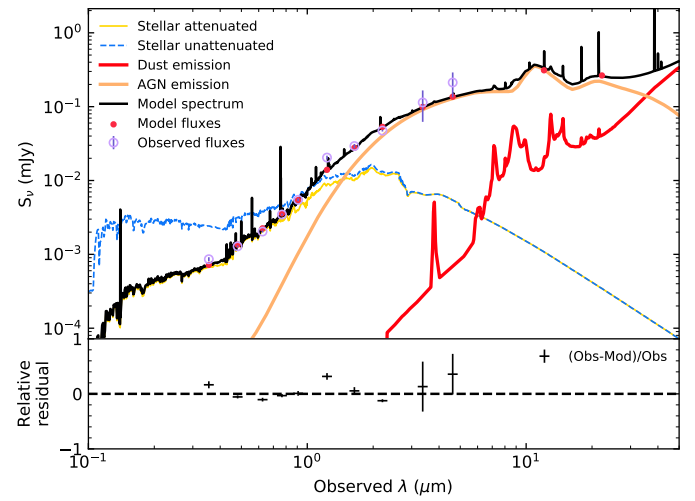
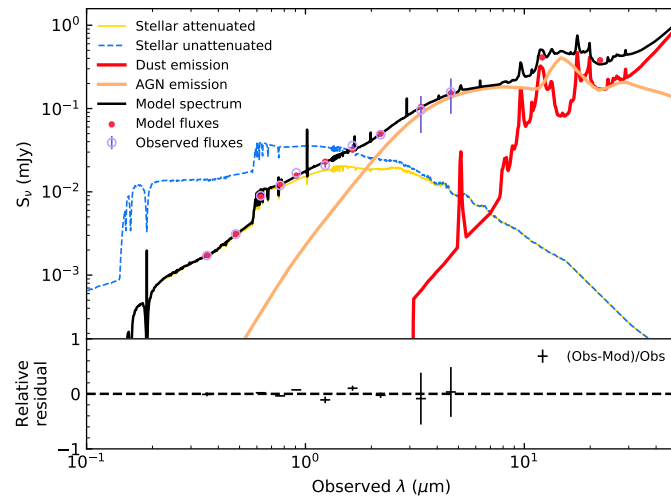
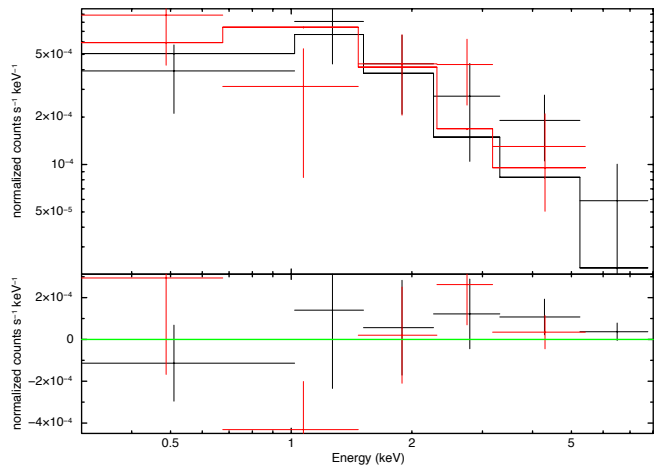
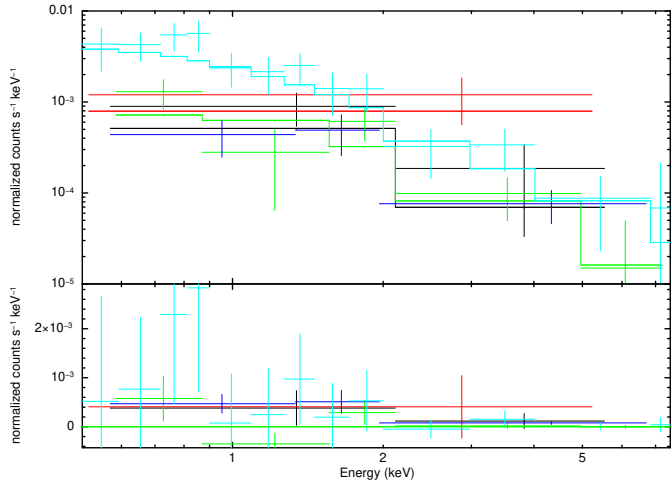


Fig. A.45: J021837.2-060654 (2,2,0), z=0.943

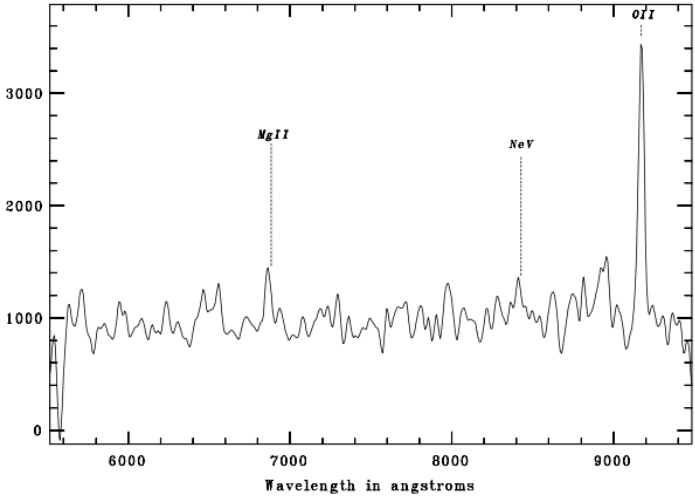


Fig. A.46: J022149.9-045920 (2,2,2), z=1.461

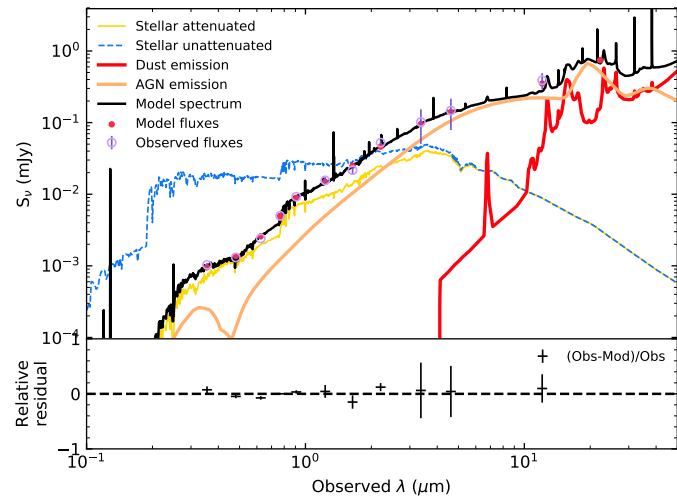
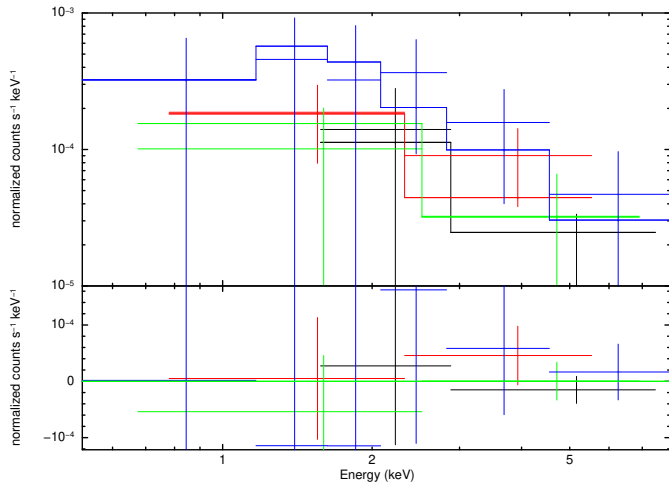


Fig. A.47: J020311.3-063534 (2,2), $z=1.05$